A&A 520, A20 (2010)
DOI: 10.1051/0004-6361/201014283

Astronomy & Astrophysics

Molecular absorption lines toward star-forming regions: a comparative study of HCO^+, HNC, HCN, and CN⋆,⋆⋆

B. Godard[1,2], E. Falgarone[1], M. Gerin[1], P. Hily-Blant[3], and M. De Luca[1]

[1] LRA/LERMA, CNRS UMR 8112, Observatoire de Paris & École Normale Supérieure, Paris, France
e-mail: godard@lra.ens.fr
[2] IAS, CNRS UMR 8617, Université Paris-Sud, Orsay, France
[3] LAOG, CNRS UMR 5571, Université Joseph Fourier & Observatoire de Grenoble, Grenoble, France

Received 18 February 2010 / Accepted 20 May 2010

ABSTRACT

Aims. The comparative study of several molecular species at the origin of the gas phase chemistry in the diffuse interstellar medium (ISM) is a key input in unraveling the coupled chemical and dynamical evolution of the ISM.
Methods. The lowest rotational lines of HCO^+, HCN, HNC, and CN were observed at the IRAM-30m telescope in absorption against the λ3 mm and λ1.3 mm continuum emission of massive star-forming regions in the Galactic plane. The absorption lines probe the gas over kiloparsecs along these lines of sight. The excitation temperatures of HCO^+ are inferred from the comparison of the absorptions in the two lowest transitions. The spectra of all molecular species on the same line of sight are decomposed into Gaussian velocity components. Most appear in all the spectra of a given line of sight. For each component, we derived the central opacity, the velocity dispersion, and computed the molecular column density. We compared our results to the predictions of UV-dominated chemical models of photodissociation regions (PDR models) and to those of non-equilibrium models in which the chemistry is driven by the dissipation of turbulent energy (TDR models).
Results. The molecular column densities of all the velocity components span up to two orders of magnitude. Those of CN, HCN, and HNC are linearly correlated with each other with mean ratios $N(\mathrm{HCN})/N(\mathrm{HNC}) = 4.8 \pm 1.3$ and $N(\mathrm{CN})/N(\mathrm{HNC}) = 34 \pm 12$, and more loosely correlated with those of HCO^+, $N(\mathrm{HNC})/N(\mathrm{HCO^+}) = 0.5 \pm 0.3$, $N(\mathrm{HCN})/N(\mathrm{HCO^+}) = 1.9 \pm 0.9$, and $N(\mathrm{CN})/N(\mathrm{HCO^+}) = 18 \pm 9$. These ratios are similar to those inferred from observations of high Galactic latitude lines of sight, suggesting that the gas sampled by absorption lines in the Galactic plane has the same chemical properties as that in the Solar neighbourhood. The *FWHM* of the Gaussian velocity components span the range 0.3 to 3 km s^{-1} and those of the HCO^+ lines are found to be 30% broader than those of CN-bearing molecules. The PDR models fail to reproduce simultaneously the observed abundances of the CN-bearing species and HCO^+, even for high-density material ($100\ \mathrm{cm^{-3}} < n_\mathrm{H} < 10^4\ \mathrm{cm^{-3}}$). The TDR models, in turn, are able to reproduce the observed abundances and abundance ratios of all the analysed molecules for the moderate gas densities ($30\ \mathrm{cm^{-3}} < n_\mathrm{H} < 200\ \mathrm{cm^{-3}}$) and the turbulent energy observed in the diffuse interstellar medium.
Conclusions. Intermittent turbulent dissipation appears to be a promising driver of the gas phase chemistry of the diffuse and translucent gas throughout the Galaxy. The details of the dissipation mechanisms still need to be investigated.

Key words. astrochemistry – turbulence – ISM: molecules – ISM: kinematics and dynamics – ISM: structure – ISM: clouds

1. Introduction

Since its discovery through absorption lines in bright star spectra (Hartmann 1904), our knowledge of the interstellar medium has grown thanks to a variety of absorption line measurements. Diatomic molecules have been discovered in this hostile environment in the late 1930's and early 1940's (see references in the review of Snow & McCall 2006) and since then have been observed in the UV and visible spectral domains toward bright stars (e.g. Crane et al. 1995; Gredel 1997; Weselak et al. 2008a,b, 2009; Gry et al. 2002; Lacour et al. 2005) at increasingly high extinction values (up to $A_V \leqslant 5$, Gredel et al. 2002). Molecules are also detected at submillimetre, millimetre, and centimetre wavelengths in absorption against the continuum emission of star-forming regions (e.g. Koo 1997; Fish et al. 2003; Nyman 1983; Nyman & Millar 1989; Cox et al. 1988; Carral & Welch 1992; Greaves & Williams 1994; Neufeld et al. 2002; Plume et al. 2004; Olofsson et al. 2010, in prep.) and bright extragalactic radio sources (Liszt et al. 2008, and references therein). The picture that emerges from these measurements is complex, and the link between the structure in density and temperature, the molecular richness, and the velocity field still needs to be unraveled. In particular, the abundance of several molecules, such as CH^+ or HCO^+, are found to be at least one order of magnitude larger than those deduced from UV-dominated chemical models. In the cases of HCO^+, HNC, and HCN the abundances inferred from observations of the diffuse ISM are similar to those observed in dark clouds (Lucas & Liszt 1996, 2000; Liszt & Lucas 2001). The column densities of specific species, like HCO^+ and OH, exhibit remarkable correlations that cannot be understood in the UV-dominated chemistry.

Alternative chemical models that couple the chemical evolution of the gas to the turbulent dynamical evolution of the medium have been developed. The space time intermittency of turbulent dissipation is invoked to locally enhance the rate of highly endoenergetic reactions, otherwise blocked in the cold ISM. Turbulent dissipation in low-velocity, magneto

⋆ Based on observations obtained with the IRAM 30 m telescope. IRAM is supported by INSU/CNRS (France), MPG (Germany), and IGN (Spain).
⋆⋆ Appendices are only available in electronic form at http://www.aanda.org

Table 1. Properties of background sources, and rms noise levels of the spectra.

Source	RA(J2000) (h) (m) (s)	Dec (J2000) (°) (′) (″)	l (°)	b (°)	D^a (kpc)	σ_l/T_c [b] HCO^+ (0–1)	σ_l/T_c [b] HCO^+ (1–2)	σ_l/T_c [b] HNC (0–1)	σ_l/T_c [b] HCN (0–1)	σ_l/T_c [b] CN (0–1)
G05.88-0.39	18 00 30.4	−24 04 00	05.88	−0.39	3.8	0.021				
G08.67-0.36	18 06 18.9	−21 37 35	08.67	−0.36	4.8	0.138				
G10.62-0.38	18 10 28.7	−19 55 50	10.62	−0.38	4.8	0.049	0.206	0.043	0.035	0.064
G34.3+0.1	18 53 18.7	+01 14 58	34.26	+0.15	3.8	0.117	0.328	0.038	0.036	0.154
W49N	19 10 13.2	+09 06 12	43.17	+0.01	11.5	0.015	0.072	0.020	0.021	0.031
W51	19 23 43.9	+14 30 30.5	49.49	−0.39	7.0	0.022	0.089	0.043	0.034	0.070

Notes. [(a)] Source distance from Fish et al. (2003) who resolve the kinematic distance ambiguity. Errors are around 1.0 kpc. [(b)] σ_l/T_c is the rms noise divided by the continuum intensity of the spectra, at a frequency resolution of 40 kHz.

Table 2. Observation parameters.

Molecule	Transition	ν_0 (GHz)	T_c (K)						T_{sys} (K)					
			G05	G08	G10	G34	W49	W51	G05	G08	G10	G34	W49	W51
HCO^+	0–1	89.1885247	1.5	0.22	0.69	0.86	1.73	1.03	156	162	206	137	167	132
HCO^+	1–2	178.3750563			0.60	0.26	1.10	0.96			588	420	375	374
HNC	0,1–1,0	90.6634170			0.97	0.88	1.94	0.93			186	162	160	191
HNC	0,1–1,2	90.6635560			0.97	0.88	1.94	0.93			186	162	160	191
HNC	0,1–1,1	90.6636220			0.97	0.88	1.94	0.93			186	162	160	191
HCN	0,1–1,1	88.6304160			1.05	1.20	1.86	1.10			158	167	146	140
HCN	0,1–1,2	88.6318470			1.05	1.20	1.86	1.10			158	167	146	140
HCN	0,1–1,0	88.6339360			1.05	1.20	1.86	1.10			158	167	146	140
CN	0, 1/2, 3/2–1, 1/2, 1/2	113.1441573			0.94	0.70	1.68	0.92			280	382	275	275
CN	0, 1/2, 1/2–1, 1/2, 3/2	113.1704915			0.94	0.70	1.68	0.92			280	382	275	275
CN	0, 1/2, 3/2–1, 1/2, 3/2	113.1912787			0.94	0.70	1.68	0.92			280	382	275	275
CN	0, 1/2, 1/2–1, 3/2, 3/2	113.4881202			0.93	0.69	1.68	0.93			284	312	209	206
CN	0, 1/2, 3/2–1, 3/2, 5/2	113.4909702			0.93	0.69	1.68	0.93			284	312	209	206
CN	0, 1/2, 1/2–1, 3/2, 1/2	113.4996443			0.93	0.69	1.68	0.93			284	312	209	206
CN	0, 1/2, 3/2–1, 3/2, 3/2	113.5089074			0.93	0.69	1.68	0.93			284	312	209	206
CN	0, 1/2, 3/2–1, 3/2, 1/2	113.5204315			0.93	0.69	1.68	0.93			284	312	209	206

hydrodynamical (MHD) shocks (Flower & Pineau des Forêts 1998) or magnetized regions of intense velocity shear (Falgarone et al. 1995; Joulain et al. 1998) are promising frameworks. Turbulent mixing between the warm neutral medium (WNM) and the cold neutral medium (CNM) has also been proposed as a possibility to enhance the formation rate of specific species (Lesaffre et al. 2007). In the turbulent dissipation regions (TDR) model of Godard et al. (2009), dissipation of turbulent energy occurs in short-lived ($\sim 10^2$ yr) magnetized vortices and is responsible for long-lasting ($\sim 10^3$ yr or more) chemical signatures due to the strong thermal and chemical inertia of the diffuse gas. Following the chemical and thermal evolutions of the dissipation and relaxation phases, the TDR models reproduce the column densities of CH^+, CH, HCO^+, OH, H_2O, C_2H, and of the rotational levels of H_2 ($J \geqslant 3$), as well as their correlations, observed in the local diffuse medium.

The present study broadens the investigation of the local diffuse medium chemistry by analysing observations performed in the direction of remote star-forming regions that sample gas throughout the Galactic plane. The selected background sources are extensively studied star-forming regions, close to the Galactic plane ($|b| < 0.5°$) (e.g. Mookerjea et al. 2007). These lines of sight are also the primary targets of the Herschel-HIFI (Heterodyne Instrument for the Far Infrared) key programme PRISMAS (PRobing InterStellar Molecules with Absorption line Studies) whose objective is to advance the understanding of astrochemistry by observing species at the origin of gas phase chemistry, namely light hydrides and small molecules containing carbon. The present work is therefore anticipating future comparisons between radio and far infrared (FIR) observations.

The observations and their analysis are discussed in Sects. 2 and 3. The main results are presented in Sect. 4 and the cyanide chemistry and the predictions of 1D chemical models are discussed in Sect. 5.

2. Observations

The observations were carried out at the IRAM-30 m telescope at Pico Veleta (Spain) in August and December 2006. For the sources listed in Table 1 (with their Galactic coordinates and their distance from the Sun), we observed in wobbler-switching mode:

- the $J = 0–1$ absorption lines of HCO^+ and HNC,
- the $F = 1–1$, $1–2$ and $1–0$ hyperfine components of the $J = 0–1$ absorption line of HCN, and
- the $F = 3/2–1/2$, $1/2–3/2$, $3/2–3/2$, $3/2–5/2$, and $1/2–1/2$ hyperfine components of the $J = 0–1$ absorption line of CN.

We used the IRAM-30 m SIS receivers tuned in SSB (single side band) mode, with rejection of the image bands larger than 15dB. The spectra were obtained using the VESPA correlator at a frequency resolution of 40 kHz. The rms pointing accuracy of the telescope checked on nearby continuum sources was 3″ and the integration time ranged between 11 and 59 min. Between 88 and 113 GHz, the forward and main beam efficiencies were of 0.95 and 0.75, the spectral resolution and the half power beam width range from ∼0.13 km s^{-1} and 28″ to ∼0.10 km s^{-1} and 22″ respectively. The observation parameters are listed in Table 2.

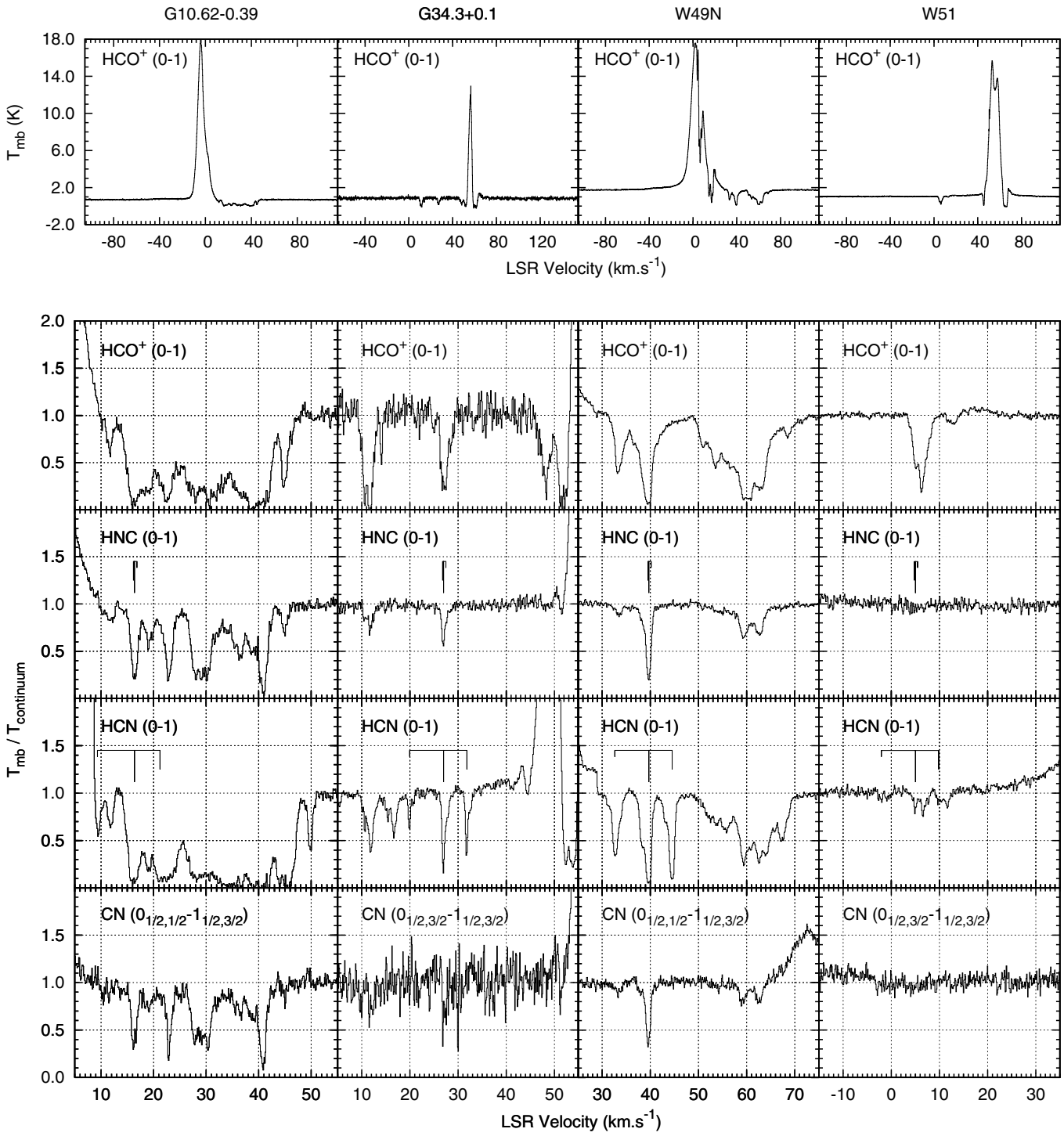

Fig. 1. Absorption profiles observed in the direction of G10.62-0.39, G34.3+0.1, W49N, and W51 in the ground state transitions of HCO^+, HCN, HNC, and CN. The hyperfine structure (relative positions and relative LTE line strength) of the $J = 0-1$ transition of HNC and HCN are displayed. The broad velocity coverage of the upper panels illustrates the quality of the baseline and the complexity of the emission and absorption mixture. The lower panels display the velocity structure of the absorption features in more details. All the spectra of the lower panels have been normalized to the continuum temperature.

The gain receiver stability, and therefore the uncertainty on the continuum level, T_c, is estimated by comparing the continuum levels from several spectra in the vicinity of the different lines. For the same frequency ranges, they differ by 0.1 to 0.3 K (see Table 2). The uncertainty on the continuum level therefore ranges between 10 and 30%.

Figure 1 displays a selection of spectra obtained after data reduction using the GILDAS-CLASS90 software[1] (Hily-Blant et al. 2005). We focus on the absorption part of the spectra,

[1] See http://www.iram.fr/IRAMFR/GILDAS for more information about GILDAS softwares.

outside the line emission of the star-forming region, since we are interested in the velocity structure and properties of the absorbing gas. In several cases, in order to extract as much information on the absorption lines as possible, the emission in wings of strong lines from the background source was removed using polynomial and exponential fitting routines.

As shown in Fig. 1, the absorption spectra are highly structured. While all the background sources are in the Galactic plane along lines of sight that cross the molecular ring and the Sagittarius spiral arm once (except that toward W49N which crosses it twice), the number of absorption features is highly variable from one source to another: ranging from 1 to 20 components. Optical depths, defined as

$$\tau = -\ln\left(\frac{T}{T_c}\right), \quad (1)$$

are also highly variable from one species to another; several components are only detectable in HCO^+, and the CN spectra are unequivocally less overcast than all the other spectra. Complementary data have been obtained with the PdBI interferometer in the direction of W49N and W51 (Pety et al., in prep.).

The hyperfine components of the $J = 0-1$ absorption lines of HNC (Bechtel et al. 2006) are too close to be individually resolved given the significant velocity dispersion of the gas. The hyperfine structure causes a systematic broadening that depends on the *FWHM* (full width at half maximum) $\Delta\upsilon_{\rm real}$ of the velocity component: the broadening $\Delta\upsilon - \Delta\upsilon_{\rm real}$ ranges[2] between 0.19 and 0.035 km s^{-1} for line *FWHM* varying from 0.3 to 3 km s^{-1}. In the case of HCN and CN (0-1), the separation of the hyperfine components is larger than most linewidths but the large number of velocity features along the lines of sight G10.62-0.38 and W49N induces a blending of the hyperfine components.

While absorption features above the noise level appear at all widths, down to the velocity resolution, we have not analysed the spectra to that level: every feature we detect spans at least 3 spectrometer channels, between 0.3 and 0.4 km s^{-1} depending on the frequency.

3. Analysis

3.1. Excitation temperatures

We observed the HCO^+ (1–2) line toward 4 of the 6 sources listed in Table 1. As shown in Fig. 2, which displays the opacities $\tau_{HCO^+(0-1)}$ and $\tau_{HCO^+(1-2)}$ in the absorption lines channel by channel, the rms noise levels are low enough to compute accurate values of the excitation temperature toward W49N and W51. Toward G10.62-0.39 and G34.3+0.1, the correlation between $\tau_{HCO^+(0-1)}$ and $\tau_{HCO^+(1-2)}$ is looser and could be due to actual variations of the excitation temperature along the line of sight.

However, for the sake of simplicity, we assume that the absorbing gas on each line of sight is defined by a single excitation temperature $T_{\rm ex}$, derived as

$$\frac{1-\exp\left(-h\nu_2/kT_{\rm ex}\right)}{\exp\left(h\nu_1/kT_{\rm ex}\right)-1} = \frac{\int\tau_2 {\rm d}\upsilon}{\int\tau_1 {\rm d}\upsilon}\left(\frac{\nu_2}{\nu_1}\right)^3 \frac{g_{\rm u1}A_{\rm ul1}}{g_{\rm u2}A_{\rm ul2}}, \quad (2)$$

where τ_1 and τ_2 are the line opacities per unit velocity, ν_1 and ν_2 the rest frequencies, $g_{\rm u1}$ and $g_{\rm u2}$ the upper level degeneracies, and $A_{\rm ul1}$ and $A_{\rm ul2}$ the Einstein's spontaneous emission coefficients of the molecular transitions HCO^+ (0–1) and (1–2) respectively. The results are listed in Table 3. For all sources,

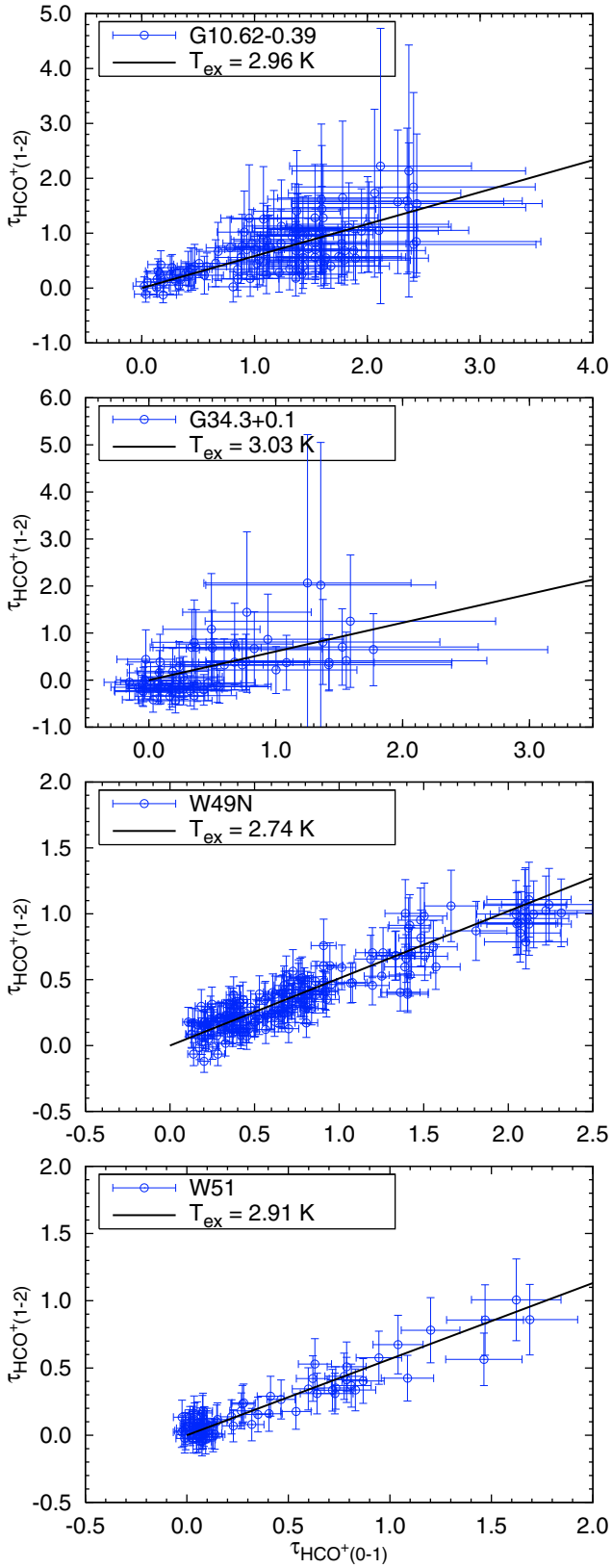

Fig. 2. HCO^+ (1–2) opacities as a function of HCO^+ (0–1) opacities. The lines are the results of linear regressions whose only parameter is the excitation temperature $T_{\rm ex}$.

[2] This result on the line profile broadening is derived from the analysis of 560 synthetic spectra taking into account the hyperfine structure of HNC (line strength and velocity structure).

Table 3. Excitation temperatures inferred from the $\tau_{HCO^+(1-2)}/\tau_{HCO^+(0-1)}$ ratio.

Source	T_{ex} (K)	errors[a] (K)	
		+	−
G10.62-0.38	3.0	1.4	0.5
G34.3+0.1	3.0	8.4	0.8
W49N	2.7	0.8	0.4
W51	2.9	1.1	0.5

Notes. [(a)] The errors are derived from the results of numerical calculation which do not take into account the lower limit of 2.73 K set by the cosmic microwave background.

T_{ex} is found close to the temperature of the cosmic microwave background $T_{CMB} = 2.73$ K.

These low excitation temperatures suggest that HCO^+, HNC, and HCN, whose dipole moments are similar, are radiatively rather than collisionally excited. Using the Large Velocity Gradients (LVG) code by Schilke (private comm.), we obtain an upper limit on the gas density: $n_H < 10^4$ cm^{-3}. This constraint is not stringent because of the large critical densities of the transitions ($\sim 10^5$ and $\sim 10^6$ cm^{-3} for HCO^+ (1–0) and HNC and HCN (1–0) respectively).

Estimates of the gas densities are provided by the LVG analysis of emission lines observed at the velocities of the absorption components. Toward W49N, ^{12}CO and ^{13}CO(1–0) and (2−1) line observations provide H_2 densities all close to 5×10^3 cm^{-3} (Vastel et al. 2000). Including the CI $^3P_1 - ^3P_0$ line in the analysis of the CO lines, Plume et al. (2004) find lower densities, ranging between 1500 and 3000 cm^{-3}. In the following, we therefore adopt $n_H < 5 \times 10^3$ cm^{-3} as an upper limit of the gas density causing the absorption features.

3.2. Decomposition of the spectra into Gaussian components

The decomposition of the spectra in velocity components and the resulting column densities are inferred from a multi-Gaussian fitting procedure based on the Levenberg-Marquardt algorithm and the following sequence.

- One of the absorption spectra is decomposed without a priori into the minimal number of Gaussians required to fit the data within the observational errors. We preferentially use the CN (0–1) transition because its hyperfine structure provides a valuable constraint on the line centroids.
- Based on the results of the previous step, the algorithm is then applied recursively to the others absorption spectra, ruling out a shift by more than a resolution element between the velocity components of each molecular species. In a few cases, a shift of at most 4 ($\sim$0.5 km s^{-1}) resolution elements is allowed because it ensures the convergence of the fitting routine: for example in regions of the spectra where many components are blended, as in the HCN (0–1) data at 59.5 km s^{-1} toward W49N.

Thus, for each transition, the observed line profile (line/continuum) is written:

$$\frac{T_{mb}}{T_c}(\upsilon) = \exp\left[-\sum_{j=1}^{N_c}\sum_{k=1}^{N_h} \alpha_h(k)\,\tau_0(j)\,e^{-\frac{1}{2}\left[\frac{\upsilon-\upsilon_0(j)-\upsilon_{0h}(k)}{\sigma_\upsilon(j)}\right]^2}\right] \quad (3)$$

where T_{mb} and T_c are the main beam and the continuum temperatures, N_c and N_h are the numbers of components and hyperfine transitions[3], τ_0, υ_0 and σ_υ are the Gaussian parameters, and α_h and υ_{0h} are the LTE and optically thin line strengths relative to a reference hyperfine transition and the velocity shift associated to each hyperfine transition. As described in Appendix A, the column density associated to each velocity component is then derived assuming a single excitation temperature T_{ex} for all the levels of a given molecule.

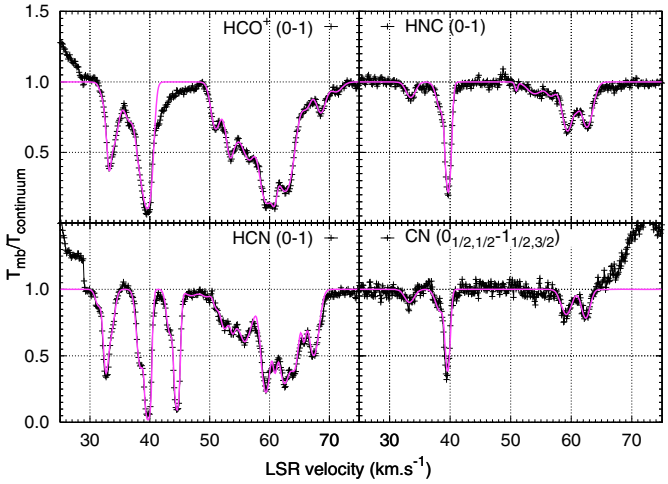

Fig. 3. Observational data (black points) compared to the multi-Gaussian decomposition (thick purple line) of the HCO^+, HNC, HCN, and CN (0–1) absorption spectra observed toward W49N.

For the components which are either saturated or too weak to be singled out by the fitting procedure, limits on the column densities are derived from the integrated optical depth over the corresponding velocity range. All the results are listed in Tables A.1–A.4 of Appendix A and, as an example, the outcome of the multi-Gaussian decomposition, applied to the absorption lines observed toward W49N, is shown in Fig. 3. We find that the widths of the Gaussian components have a continuous distribution with values ranging from 0.3 km s^{-1} to 3.5 km s^{-1}, independently of the source or the molecular species. The peak optical depths range between 0.06 and 2.2 and the inferred column densities per velocity component span more than one order of magnitude on each line of sight.

3.3. Systematic errors on calculation of column densities

The uncertainties given in Tables A.1–A.4 are the formal 1-σ errors derived from the diagonal elements of the covariance matrix and do not take into account the systematic errors introduced by: (1) the finite velocity resolution; (2) the uncertainty on the excitation temperatures (see Table 3); and (3) the uncertainty on the continuum level.

We show in Appendix B that the finite velocity resolution introduces an error on the column densities smaller than 12%. Table 3 gives the uncertainties on the excitation temperature of the lowest rotational levels of HCO^+, that affects the partition function, hence the column densities. Toward G10.62-0.38, W49N, and W51, the uncertainties on T_{ex} are small, providing uncertainties on the column densities $<^{+50\%}_{-10\%}$. Toward G34.3+0.1, the inferred column densities could be underestimated by a factor of 3.

[3] N_h depends on the molecule.

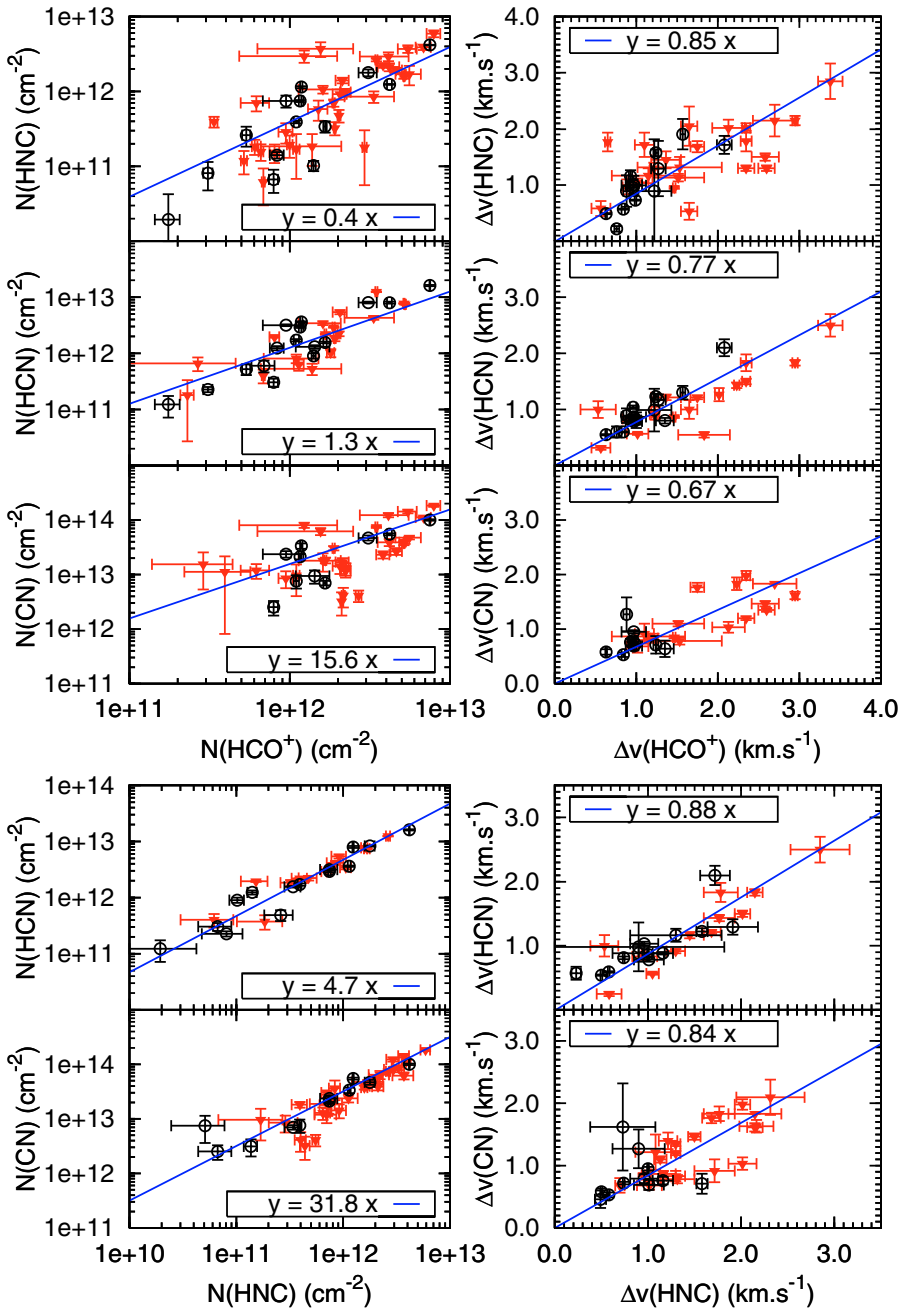

Fig. 4. Comparisons of the column densities (*left panels*) and the *FWHM* (*rigth panels*) of HCO^+, CN, HCN, and HNC. The red filled symbols are from this work. The black open symbols are from Lucas & Liszt (1996) and Liszt & Lucas (2001). The solid lines result from a linear regression of the data of the present work unweighted by the fractional errors on N and Δv : $Y = \alpha X$.

Finally, the uncertainty $\epsilon = \delta T_c/T_c$ on the continuum temperature (see Sect. 2) introduces an error $\delta\tau$ on the calculation of the optical depths:

$$\delta\tau \sim \epsilon - \ln(1 + \epsilon e^{\tau}) . \quad (4)$$

This error is larger, in most cases, than those inferred from the fitting procedure, and for $\epsilon = 10\%$ the corresponding uncertainty on the column densities ranges from 16% to 62% when τ_0 varies between 0.5 and 2. All components with $\tau_0 > 2.2$ are thus considered as saturated. The components at 16 and 41 km s^{-1} of the G10.62-0.38 HCO^+(0–1) spectrum are the only ones that fall in this category.

When all uncertainties are taken into account, the column densities are determined within a factor of 2, and within a factor of 3 for the absorption lines observed toward G34.3+0.1.

4. Results

4.1. Comparison of column densities and profile linewidths among species

Because the line centroids of a Gaussian component observed in several transitions coincide within 0.15 km s^{-1} (except for 6 components, see Appendix A, Tables A.1–A.4), we propose that the corresponding velocity component has a physical reality, in support of the comparison between the optical depths in the different molecular lines and the resulting column densities.

The column densities and linewidths of all the unsaturated velocity components are displayed in Figs. 4 and 5 for several pairs of species. These figures also include, for comparison, the results of previous studies of molecular absorption

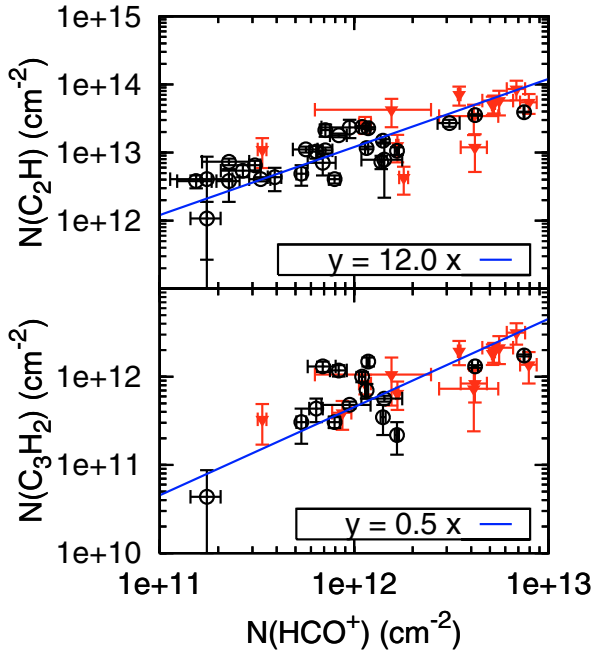

Fig. 5. Comparisons of the column densities of HCO^+, C_2H, and c–C_3H_2. The column densities of C_2H and c–C_3H_2 are from Gerin et al. (2010). The red filled symbols are from this work. The black open symbols are from Lucas & Liszt (1996, 2000). The solid lines result from a linear regression of the data of the present work unweighted by the fractional errors on $N : Y = \alpha\ X$.

lines observed toward strong extragalactic mm-wave continuum sources (Lucas & Liszt 1996, 2000; Liszt & Lucas 2001) that mostly sample diffuse gas in the Solar Neighbourhood.

Although we have not made any assumption on the nature of a Gaussian velocity component, it is remarkable that *(i)* the range of the component linewidths (0.3 to 3.5 km s^{-1}) is about the same in both data sets, and *(ii)* the range of column densities of most molecular species (up to two orders of magnitude) is also similar in both sets. This result suggests that the gas components sampled at high galactic latitude and toward the inner Galaxy share common kinematic properties. In addition the rotation curve in the first quadrant provides displacements ∼70−100 pc/km s^{-1}: therefore, if we assume that the induced spreading of the velocity centroids is responsible for the observed linewidths, a component of 3 km s^{-1} (resp. 0.3 km s^{-1}) would have a size of 300 pc (resp. 30 pc). This would correspond to densities $n_{\rm H} < 40$ cm^{-3}, below our estimates (see Sect. 4.3). Hence, the linewidths of the components are likely due to turbulence rather than differential rotation of the galactic plane. In the following, we compare the chemical and kinematic properties of these two ensembles. While the thick lines in Figs. 4 and 5 result from a linear regression unweighted by the fractional errors on the fitting parameters, the values given below come from weighted[4] averages.

- Concerning the column densities of HNC, HCN, and CN, Liszt & Lucas (2001) found tight linear correlations along lines of sight at high Galactic latitude, namely N(HCN)/N(HNC) = 4.8 ± 1.1 and N(CN)/N(HNC) = 33 ± 12. In comparison the mean ratios of the present work are N(HCN)/N(HNC) = 4.8 ± 1.4 and N(CN)/N(HNC) = 34 ± 12.

[4] A weighted average makes more sense numerically but tends to favour the high column density points. In practice, both evaluations (weighted and unweighted) are meaningful since the errors are not known with high accuracy (see Sect. 3.3).

- Figure 4 (top) shows that the correlations of the CN-bearing molecules with HCO^+ are looser and probably non linear with mean ratios: N(HNC)/N(HCO^+) = 0.5 ± 0.3, N(HCN)/N(HCO^+) = 1.9 ± 0.9, and N(CN)/N(HCO^+) = 18 ± 9.
- Last, the loose linear relation between the column densities of C_2H and HCO^+ observed in Fig. 5 corresponds to a mean ratio $N(C_2H)/N(HCO^+)$ = 8.3 ± 5.6 to be compared with $N(C_2H)/N(HCO^+)$ = 14.5 ± 6.7 obtained by Liszt & Lucas (2001).

The linewidths of the Gaussian components of the HCO^+, CN, HCN, and HNC line profiles are close to be the same. We find that the CN, HCN, and HNC line profiles are systematically narrower than those of HCO^+ (by a factor of 0.7 to 0.9). In Fig. 4, the CN and HCN line profiles appear to be narrower than those of HNC (by a factor of 0.8 to 0.9) but this result is mostly due to the hyperfine structure of HNC that has not been taken into account in the decomposition. Once the correction discussed in Sect. 2 is applied, the significance of the linewidth difference disappears. The profiles of C_2H and C_3H_2 have been studied with a different method, and the components identified are not the same as those in the present study (Gerin et al. 2010).

4.2. Estimation of the total hydrogen column densities along the lines of sight

In order to be able to compare the data to chemical models, molecular abundances must be derived and column densities of hydrogen measured. In particular, it is essential to determine whether the wide dynamic ranges over which the correlations are observed (Figs. 4 and 5) are related to variations of the total column density of the gas sampled or/and of the physical and chemical conditions in the absorbing gas. The main difficulty is to estimate the fraction of molecular hydrogen that is not directly observable. Using λ21 cm observations of HI, λ9 cm and λ0.3 mm observations of CH, and the remarkable correlation between CH and H_2, $N(CH)/N(H_2) = 4.3 \times 10^{-8}$ (Liszt & Lucas 2002), we evaluate the total amount of gas $N_{\rm H} = N({\rm H}) + 2N(H_2)$ along the galactic lines of sight, as in Godard et al. (2009) for the lines of sight studied by Liszt & Lucas (2001). The HI column densities are inferred from VLA λ21 cm absorption line observations (Koo et al. 1997; Fish et al. 2003). Wherever possible, we derive $N(H_2)$ from CH observations (at 9 cm by Rydbeck et al. 1976; at 1 THz by Gerin et al., in prep.).

An independent estimate of the total column density of gas toward the star-forming regions is inferred from the analysis of the 2MASS survey (Cutie et al. 2003). Marshall et al. (2006) have measured the near infrared colour excess in large areas of the inner Galaxy ($|l| < 100°$, $|b| < 10°$) to obtain the visible extinctions ($A_V \sim 10 A_K$), providing an estimate of the total hydrogen column density along the lines of sight.

Table 4 lists the HI (and H_2, where available) column densities in selected velocity intervals, as well as the total hydrogen column densities inferred from extinction. However the uncertainties on these estimations are large: (1) the error on the N(CH) – $N(H_2)$ relation is about a factor of 3 (Liszt & Lucas 2002); (2) this correlation has been established in the local diffuse medium but has never been observed in the inner Galaxy material; (3) because of the low resolution of the 2MASS survey (∼15 arcmin), the error on the total hydrogen column density (computed as the standard deviation of the extinction measured along the four closest lines of sight surrounding a given source) is larger than 30%; and (4) The HI column densities

Table 4. HI, H_2 and total hydrogen column densities.

Source	v_0 (km s^{-1})	Δv (km s^{-1})	N(H)^a (cm^{-2}) $\times 10^{21}$	$N(H_2)^c$ (cm^{-2}) $\times 10^{21}$	N_H^d (cm^{-2}) $\times 10^{21}$
W51	6.2	5.6	1.27	0.47	2.3
	11.8	6.0	0.58		
Source	v_{min} (km s^{-1})	v_{max} (km s^{-1})	N(H)^b (cm^{-2}) $\times 10^{21}$	$N(H_2)^c$ (cm^{-2}) $\times 10^{21}$	N_H^d (cm^{-2}) $\times 10^{21}$
G05.88-0.39	−31.3	−10.0	1.59		16
	−10.0	4.0	>6.68		
	4.0	20.0	5.87		
	20.0	29.3	>3.86		
G08.67-0.36	−1.7	11.3	4.80		14
	11.3	25.7	5.32		
	25.7	45.3	>9.62		
G10.62-0.38	11.3	25.0	3.53		17
	25.0	30.6	2.61	15.8	
	30.6	47.3	5.54		
G34.3+0.1	−2.5	7.1	0.54		9
	7.1	20.0	2.01		
	20.0	34.1	4.42		
W49N	30.0	50.0	6.95	1.6	23
	50.0	78.2	7.23	4.0	

Notes. [(a)] Gaussian decomposition from Koo (1997). The column densities have been scaled to a spin temperature of 100 K. [(b)] Inferred from the absorption profiles observed by Fish et al. (2003) with the VLA interferometer. A spin temperature of 100 K is assumed. [(c)] Estimation from the CH emission lines observed by Rydbeck et al. (1976) toward W51 and W49N, the CH absorption lines observed by Gerin et al. (in prep.) toward G10.62-0.38, and the correlation between CH and H_2, $N(CH)/N(H_2) = 4.3 \times 10^{-8}$ (Liszt & Lucas 2002). [(d)] From models of the extinction at 2 μm by Marshall et al. (2006).

inferred from VLA λ21 cm absorption line observations are directly proportional to the assumed spin temperature. Hence, while the two determinations agree with each other within 15% toward W51 and W49N, they differ by at least a factor of 2 toward G10.62-0.38.

According to the extinction measurements, the lines of sight sample between 1.3 (W51) and 12.5 (W49N) magnitudes of gas. The total velocity coverage of the absorption features is ~10 km s^{-1} toward W51 and 48 km s^{-1} toward W49N. Therefore, the average hydrogen column density *per velocity unit* is only twice larger along the line of sight toward W49N than along that toward W51. It is therefore possible to estimate the molecular abundances relative to the total hydrogen column density N_H for each velocity component, assuming that N_H scales with their linewidth according to $N_H/\Delta v = 2.2$ and 4.7×10^{20} cm^{-2}/km s^{-1} toward W51 and W49N respectively. This is equivalent to assuming a uniform HI optical depth in the gas components where we observe molecular absorption. Such an approximation underestimates the HI column density per unit velocity by no more than a factor 2. The total hydrogen column densities estimated with this method and given in Table A.1 for W49N and W51 are smaller by only 50% than those inferred from IR extinction. We therefore estimate that the total H column density per velocity component on these two lines of sight does not exceed 1.5 magnitude (or about 2.5×10^{21} cm^{-2}). This result suggests that the HCO^+ abundance in the different velocity components, defined as $X(HCO^+) = N(HCO^+)/N_H$, ranges between 5×10^{-10} and 5×10^{-9} toward both W49N and W51. For HCN, the scatter of abundances is also an order of magnitude among the components, with values ranging between 2×10^{-9} and 3×10^{-8} for W49N. A similar scatter is also found for HNC with abundances ~10 times smaller.

In summary, since the column densities of the Gaussian components span less than two orders of magnitude while their linewidths span only a factor ~10 (between 0.3 and 3.4 km s^{-1}), actual fluctuations of molecular abundances are therefore observed among the components.

4.3. Physical properties of the gas seen in absorption

The above average description is crude and is only meant to ascribe an average column density to a velocity interval, ignoring velocity crowdings: the lines of sight toward distant star-forming regions sample gas components with a broad distribution of densities, velocity dispersions, and column densities. We have shown that the upper limit on the gas density is $n_H < 5 \times 10^3$ cm^{-3} (cf. Sect. 3.1) and that the total column densities per velocity components N_H are at most of the order of a few magnitudes, similar to those obtained along the high latitude lines of sight observed by Liszt & Lucas (2001). According to the definitions of Snow & McCall (2006), the gas sampled by these lines of sight is a mixture of diffuse ($n_H < 500$ cm^{-3} with a shielding from the UV field $A_V < 1$) and translucent gas (500 cm^{-3} $< n_H <$ 5000 cm^{-3} and a shielding $1 < A_V < 2$).

Allowing the gas density to range between 30 cm^{-3} and 5×10^3 cm^{-3}, the total N_H per velocity component of a few magnitudes translates into sizescales ranging between ~0.2 and ~30 pc. It is interesting that the corresponding range of velocity dispersions inferred from the linewidth-scale relation in the diffuse molecular gas (Falgarone et al. 2009) is ~0.2–5 km s^{-1}, very close to the observed range of component velocity dispersions. It suggests that the mixture of diffuse and transluscent gas sampled by these lines of sight is entrained in the turbulent interstellar cascade. Although one velocity component is not necessarily a cloud, the linewidth-scale relation ascribes a sizescale to each velocity dispersion, $\Delta u \sim 1(l/1\ \mathrm{pc})^{1/2}$ km s^{-1}. Therefore, different molecular species present in a given velocity component of width Δu are colocated within ~0.1 pc (if $\Delta u = 0.3$ km s^{-1}) and 9 pc (if $\Delta u = 3$ km s^{-1}). It is the correlation of molecular species, observed at these grains, that we will now confront to the predictions of different numerical codes.

In the following sections, we therefore study the chemistry of diffuse and translucent gas, and we compare the observed column densities to the results of PDR (PhotoDissociation Region) and TDR (Turbulent Dissipation Region) models.

5. Comparison of observations to model predictions

5.1. Introduction to the PDR and TDR models

The comparison of the PDR and TDR models has been discussed in detail in Godard et al. (2009). We recall here the main differences between the two approaches.

The PDR model is a 1-dimensional chemical model in which a static slab of gas of uniform density and given thickness (or total column density of gas, noted N_H in the following) is illuminated by the ambient interstellar radiation field either on one side or on both sides (Le Petit et al. 2006). The computed column

density of a molecular species to be compared to the observed values is therefore an integral performed over the slab thickness along a direction perpendicular to its surface.

The TDR code is a 1-dimensional model in which the chemical and thermal evolution of a turbulent dissipative burst – namely a magnetized vortex – is computed. The dynamics and lifetime of the magnetized vortices are controlled by the turbulent rate of strain a (in s^{-1}), the gas density n_H (in cm^{-3}), and the maximal orthoradial velocity $u_{\theta\,max}$ (in $cm\,s^{-1}$). A random line of sight crossing several dissipative regions is then modelled by taking into account: the averaged turbulent dissipative rate observed in the CNM, and the long-lasting thermal and chemical relaxation stage that follows any dissipative burst. The resulting line of sight therefore intercepts three kinds of diffuse gas: (1) mainly the ambient medium (the corresponding filling factor is larger than 90%) in which the chemistry is driven by the UV radiation field; (2) the active vortices where the gas is heated and the chemistry is enhanced by the dissipation of turbulent energy; and (3) the relaxation stages where the gas previously heated cools down to its original state. Because of the strong experimental (Mouri et al. 2007; Mouri & Hori 2009) and observational (Crovisier 1981; Joncas et al. 1992; Miville-Deschênes et al. 2003; Haud & Kalberla 2007) constraints on $u_{\theta\,max}$, only two main parameters govern the TDR model: the turbulent rate of strain that describes the coupling between the large and small scales of turbulence and the gas density. However, both parameters are not independent because of the constraint imposed by the observed turbulent energy available in the CNM, namely $\overline{\varepsilon}_{obs} \sim 2 \times 10^{-25}$ $erg\,cm^{-3}s^{-1}$ (Falgarone 1998; Hily-Blant et al. 2008). As a result, the influence of the parameters on the TDR model, fully discussed in Godard et al. (2009), is complex.

- The gas density n_H affects the chemistry itself and has several impacts due to the dynamics and the geometry of the line of sight. For the range of parameters explored here, the dissipation of turbulent energy over one vortex is mainly due to ion-neutral friction and varies roughly as n_H^2; the vortex radius varies as $n_H^{-1/2}$, and their number along the line of sight as n_H^{-2}.
- While the dissipation of turbulent energy over one vortex and the number of vortices along the line of sight are nearly independent of the turbulent rate of strain a, their size and their lifetime vary roughly as $a^{-1/2}$ and a respectively.

For both models and as shown in Table C.1 of Appendix C, the nitrogen gas phase chemistry has been updated according to the recent measurements and rate review. However, neither the PDR nor the TDR chemical networks take into account the nitrogen grain surface chemistry: this assumption will be discussed in Sect. 6.1.

5.2. Gas phase nitrogen chemical networks in the PDR and TDR models

The networks of dominant reactions in the nitrogen gas phase chemistry are shown in Figs. C.1 and C.2 (Appendix C). While in both models, photodissociation largely dominates the destruction mechanisms of CN-bearing molecules, there are several pathways that lead to their production.

In the PDR model (Federman et al. 1994; Boger & Sternberg 2005), two main formation routes are at work. The first involves the hydrogenation chain of carbon and the formation of CH and CH_2, which in turn, leads to CN and HCN via the neutral-neutral reactions:

$$CH + N \rightarrow CN + H \tag{5}$$

and

$$CH_2 + N \rightarrow HCN + H. \tag{6}$$

The second one involves the hydrogenation chain of nitrogen and the formation of NH and NH_2, followed by the ion-neutral reaction chains

$$NH \xrightarrow{C^+} CN^+ \xrightarrow{H_2} \begin{matrix} HCN^+ \\ HNC^+ \end{matrix} \xrightarrow{H_2} HCNH^+ \tag{7}$$

and

$$NH_2 \xrightarrow{C^+} HCN^+ \xrightarrow{H_2} HCNH^+, \tag{8}$$

the dissociative recombination of $HCNH^+$, and the photodissociation of HCN and HNC.

In the TDR model, because of both the differential rotation at the edge of the vortex and the ion-neutral drift, the gas is locally heated, and several key endoenergetic reactions such as

$$C^+ + H_2 \rightarrow CH^+ + H \qquad -\Delta E/k = 4640\ K \tag{9}$$

open up. A warm nitrogen chemistry is triggered locally (Fig. C.2, Appendix C). Although the temperatures reached in a vortex ($\sim 10^3$ K) are not sufficient to activate the reaction

$$N + H_2 \rightarrow NH + H \qquad -\Delta E/k = 16\,606\ K \tag{10}$$

(whose rate becomes large enough only at 7000 K, Crawford & Williams 1997), the pathways leading to the production of N bearing species are deeply modified and their abundances increase considerably. The opening of the endoenergetic route $C^+ + H_2$, that forms CH^+ and then $CH_2{}^+$ and $CH_3{}^+$ by fast reaction with H_2, triggers in turn the enhancement of the production of CN-bearing molecules through the ion-neutral reaction chains

$$CH^+ \xrightarrow{N} CN^+ \xrightarrow{H_2} \begin{matrix} HCN^+ \\ HNC^+ \end{matrix} \xrightarrow{H_2} HCNH^+, \tag{11}$$

$$CH_2^+ \xrightarrow{N} HCN^+ \xrightarrow{H_2} HCNH^+, \tag{12}$$

and

$$CH_3^+ \xrightarrow{N} HCNH^+, \tag{13}$$

followed by the dissociative recombination of $HCNH^+$ and the photodissociation of HCN and HNC. Therefore, the key species here is CH_3^+. Its reaction with atomic nitrogen is able to significantly enhance the production of $HCNH^+$ compared to that in the PDR models, leading to HCN, HNC, and CN. Similarly, $CH_3{}^+$ is responsible for the enhancement of HCO^+ by its reaction with atomic oxygen (see the discussion in Godard et al. 2009).

5.3. Comparison of PDR model predictions with the observations

To explore the role of the parameters in the Meudon PDR code (Le Petit et al. 2006) we computed several two-sided illuminated PDR models, as follows:

- based on the results of Sect. 4.2, the total column density of gas in the slab is either $N_H = 1.8 \times 10^{21}$ or 3.6×10^{21} cm^{-2} (corresponding to 1 and 2 magnitudes respectively);

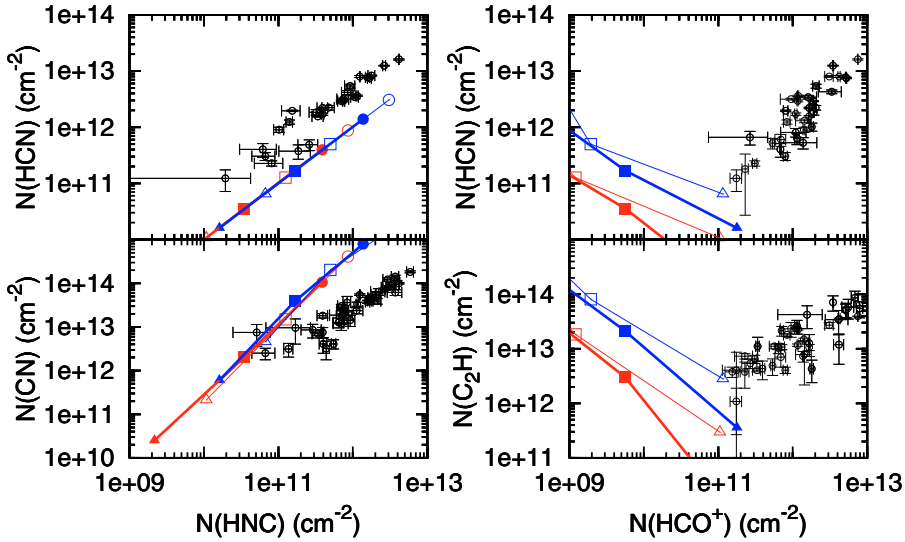

Fig. 6. Observations compared to the predictions of PDR models. The data (open circles) are from Lucas & Liszt (2000), Liszt & Lucas (2001), Gerin et al. (2010), and this work. The PDR models are computed for several densities: 10^2 (triangles), 10^3 (squares), and 10^4 (circles) cm^{-3}. Red and blue curves correspond to N_H = 1 and 2 magnitudes respectively. Thin (empty symbols) and thick (filled symbols) curves correspond to χ = 1 and χ = 3.

- two values of χ are considered, χ = 1 and χ = 3, in order to bracket the ambient UV radiation field found to vary between the Solar Neighbourhood (~8.5 kpc from the Galactic centre) and the molecular ring (~4 kpc from the Galactic centre) by a factor ~3 (Moskalenko et al. 2006);
- the gas density is set to $n_H = 10^2$, 10^3, and 10^4 cm^{-3}.

Each model was computed assuming a cosmic ray ionisation rate $\zeta = 3 \times 10^{-17}$ s^{-1} (Dalgarno 2006). The results on the column densities and the column density ratios of HCO^+, HCN, HNC, CN, and C_2H are given in Fig. 6 which also displays, for comparison, the ranges of observed values.

This figure shows that the constraints provided by the CN-bearing molecules and by HCO^+ cannot be reconciled in the framework of this model. On the one hand, both the range of column densities and column density ratios of CN, HCN, HNC, and C_2H can be explained by PDR models for $N_H > 1.8 \times 10^{21}$ cm^{-2} and a gas density larger than 300 cm^{-3}. But on the other hand, for the same range of density, not only the predicted correlation between the column densities of CN and HNC is clearly non-linear and mismatch the observed value by a factor larger than 10, but the column densities of HCO^+ are also underestimated by at least one order of magnitude.

As expected, if the mean interstellar UV radiation field increases, the column densities of CN, HCN, HNC, and C_2H decrease because the photodissociation is the main destruction process of all these molecules. Oppositely, when χ is multiplied by 3, the temperature at the edge of the PDR is twice larger and the $O + H^+$ charge exchange reaction (with an endothermicity $\Delta E/k$ of 227 K) is enhanced. Since this reaction is at the root of the formation of HCO^+ in low density UV-dominated gas phase chemistry (Godard et al. 2009) and since the main destruction mechanism of HCO^+ is its dissociative recombination (whose rate is independent of χ), the column density of HCO^+ increases (see Fig. 6). All those behaviours holds for the ranges of density and radiative conditions explored in Fig. 6.

The dependence of the results on the cosmic ray ionisation rate ζ is slightly more complex. When ζ is multiplied by 10, the abundances of H^+ and H_3^+ rise by one order of magnitude[5]. Thus, both the hydrogenation chains of nitrogen and oxygen are stimulated by the reactions

$$N + H_3^+ \rightarrow NH_2^+ + H \quad (14)$$

and

$$O + H^+ \rightarrow O^+ + H \quad (15)$$

respectively, while the hydrogenation chain of carbon, initiated by the slow radiative association

$$C^+ + H_2 \rightarrow CH_2^+ + H \quad (16)$$

is independent of ζ. Therefore when ζ is multiplied by 10:

- the column density of HCO^+ increases by a factor of 10 whatever the gas density;
- since CN always originates from the carbon hydrogenation chain, its column density is independent of ζ;
- since HCN and HNC originate from the carbon hydrogenation chain at large density and from the nitrogen hydrogenation chain at low density, their column densities are independent of ζ if $n_H > 300$ cm^{-3}, and increase by a factor of 2 if $n_H < 300$ cm^{-3}.

Nevertheless, even at low density, the impact of the cosmic ray ionization rate is not sufficient enough to account for the range of column densities observed in Fig. 6.

5.4. Comparison of observations with TDR model predictions

As suggested by Godard et al. (2009) and by the present observations, we explore the TDR models in the range of parameters: $10^{-12} < a < 10^{-10}$ s^{-1} and $30 < n_H < 500$ cm^{-2} for an ambient radiation field characterized by χ = 1. Since the influence of this

[5] H^+ and H_3^+ are formed via the reaction chains $H_2 \xrightarrow{CRP} H_2^+ \xrightarrow{H_2} H_3^+$ and $He \xrightarrow{CRP} He^+ \xrightarrow{H_2} H^+$ respectively (CRP: cosmic ray particle).

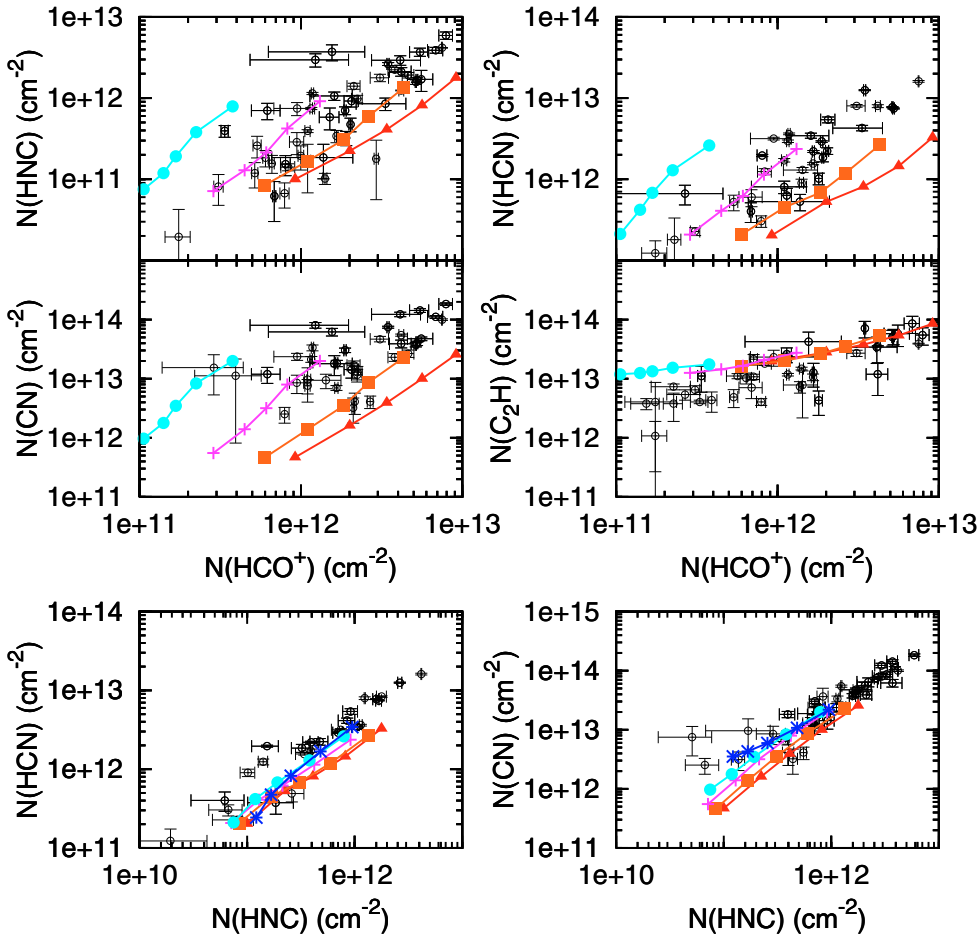

Fig. 7. Observations compared to the predictions of TDR models. The data (open circles) are from Lucas & Liszt (2000), Liszt & Lucas (2001), Gerin et al. (2010), and this work. The TDR models (filled symbols) are computed for several densities: 30 (triangles), 50 (squares), 100 (crosses), 200 (circles), and 500 (double crosses) cm^{-3}. All models are computed for $N_H = 1.8 \times 10^{21}$ cm^{-2}: note that if the total column density was larger, the model predictions would be simply multiplied by the same factor. The TDR models are computed for $A_V = 0.5$ and a varying along each curve between 10^{-12} (*top right*) and 10^{-10} s^{-1} (*bottom left*).

parameter on the results of the PDR model (see Fig. 6) seems to be small compared to the role of N_H and n_H, we did not explore a broader range of values for χ. The shielding from the ISRF is assumed uniform, $A_V = 0.5$ and the amount of gas sampled is fixed to $N_H = 1.8 \times 10^{21}$ cm^{-2}. Note that, in the TDR model, A_V is the actual UV-shielding of the gas and is no longer identical to the total hydrogen column density sampled by the line of sight (as it is the case in the PDR model).

Figure 7 displays the comparison between the observed molecular column densities and the predictions of the TDR models. Since the results of the TDR model are simply proportional to N_H, the computed values for higher (or lower) values of N_H are easily inferred from the display. TDR models, without fine tuning of the parameters, are consistent with the data. Over a broad range of turbulent rates of strain 10^{-12} $s^{-1} \leqslant a \leqslant 10^{-10}$ s^{-1} and for a gas density 30 $cm^{-3} \leqslant n_H \leqslant 200$ cm^{-3}, the absolute column densities and column density ratios of HCO^+, C_2H, CN, HCN, and HNC are reproduced. The case $n_H = 500$ cm^{-3} is ruled out because the computed HCO^+ column densities are too small compared to the observed values, even if the total hydrogen column density N_H or the averaged turbulent dissipative rate ε are multiplied by a factor of 10. For the CN-bearing species, all deriving from $HCNH^+$ during the dissipation stage, the agreement with the observations holds over a broader range of gas density: 30 $cm^{-3} \leqslant n_H \leqslant 500$ cm^{-3}. A trend, that was already found in Godard et al. (2009), is that the observed column densities are in better agreement with models of small turbulent rate of strain.

6. Discussion

6.1. Grain surface chemistry

As shown in the previous section, if only the gas phase chemistry is taken into account, the predictions of UV-dominated chemical models computed at moderate densities ($n_H < 300$ cm^{-3}) are unable to explain the observed column densities of the CN-bearing species. This result is in agreement with the previous studies of Wagenblast et al. (1993), Crawford & Williams (1997), and Liszt & Lucas (2001) which show that the predictions of purely gas phase PDR models fail by a factor of 7 to account for the CN abundances observed in the low density material toward ζ Per, and by factors of 30 and 40 to reproduce the NH abundances observed toward ζ Per and ζ Oph respectively.

In the present paper we explore the role of turbulent dissipation on the cyanide chemistry that operates via the hydrogenation chain of ionized carbon followed by the reaction chains (11),

(12), and (13). An ongoing related work is the comparison of the TDR model predictions to the Herschel-HIFI observations of nitrogen hydrides along W31C and W49N (Persson et al. 2010).

But there is an alternative possibility to the pure gas phase chemistry. It has been proposed that the grain surface chemistry dominate all the other formation processes of the ammonia NH_3, and is therefore responsible[6] for the production of NH and CN in the diffuse ISM (van Dishoeck & Black 1988). Assuming a NH_3 grain formation rate coefficient of

$$k_G = 5.4 \times 10^{-18} \left(\frac{T \ [\mathrm{K}]}{m(N) \ [\mathrm{amu}]} \right)^{0.5} \quad \mathrm{cm^3\ s^{-1}}, \tag{17}$$

corresponding to a surface reaction efficiency twice lower than that for the H_2 formation on grains, Wagenblast & Williams (1996) found that a UV dominated chemical model reproduces the CN and NH abundances observed toward ζ Per and ζ Oph. However, this approach is based on the assumption that if a nitrogen atom strikes and sticks to a grain, ammonia is quickly formed and comes off the grain. The resulting rate coeficient, namely the cross section of the grain multiplied by the average speed of nitrogen atoms, clearly sets an upper limit to the efficiency of the grain surface chemistry.

6.2. The UV radiation field

Although, as said above, the comparison of model predictions to observations is a difficult task because of the lack of information on the gas topology (density structure, division of the matter therefore shielding from the ambient UV field, homogeneity of the gas conditions among the different fragments) and the poorly known physical characteristics of what is called a "Gaussian-velocity component", we have three main constraints to guide the models.

In the Gaussian-velocity components, (i) the gas density is lower than $n_H = 5 \times 10^3$ cm^{-3}; (ii) where it is estimated, the column density of H_2 is between 0.3 and 1.3 that of atomic hydrogen (Table 4); and (iii) the *average* hydrogen column density per unit velocity interval ranges between 2 and 5×10^{20} cm^{-2}/km s^{-1}. This implies that the total hydrogen column density cannot be much larger than 4×10^{21} cm^{-2} and that the shielding from the ambient radiation field is efficient (otherwise the H_2 fraction would be small). According to PDR models, this imposes a narrow combination of the total column density N_H and ambient UV field intensity χ. We are therefore confident that the gross properties of the UV illumination of the gas in the "Gaussian velocity-components" are well estimated.

6.3. The velocity field

The fact that the widths of the HCO^+ components are systematically larger than those of the CN-bearing species suggests an involvement of the velocity field in the production and the evolution of these species. Observations in the visible domain by Lambert et al. (1990), Crane et al. (1995), and Pan et al. (2004, 2005) already showed that the CH^+ line profiles are broader and less Gaussian than those of CH, themselves broader than those of CN. It has been proposed that such behaviours are due to spatial confinement of the molecules whose production occurs hierarchically into denser and colder environments (Crawford 1995). But the differences observed among the linewidths may also bear the signatures of the dynamical processes at work in the formation of all those molecules convolved with their most different relaxation times (Godard et al. 2009). Last, the similarity between the results obtained along Galactic lines of sight and in the Solar Neighbourhood also suggests a formation mechanism weakly dependent on the ambient UV field, i.e. possibly driven for instance by the dissipation of the ubiquitous turbulence.

[6] In a UV-dominated chemistry, the main destruction route of NH_3 is its photodissociation. The product NH_2 then leads to the formation of NH and CN (see Fig. C.1).

7. Summary and conclusions

We have presented the analysis of single dish observations of mm absorption lines of HCO^+, HNC, HCN, and CN toward remote star-forming regions in the Galactic plane. The density of the gas responsible for the absorption lines is constrained by the excitation temperature of the first rotational levels of HCO^+ and, in two cases, by line emission of CO (and isotopes). An upper limit $n_H < 5 \times 10^3$ cm^{-3} is obtained. The estimation of the total column densities along the lines of sight, combined with their H_2 fraction, where known, gives an upper limit on the UV-shielding per velocity component, $A_V < 2$. These conditions suggest that the gas sampled along the lines of sight belongs to the diffuse and/or translucent media. Because the decomposition of the velocity structure into Gaussian components has been carried out recursively for all the molecules and hyperfine components, intercomparisons of molecular abundances are feasible. The inferred velocity structure will be helpful to unravel the analysis of future observations with Herschel/HIFI.

Our main result is the similarity between the column densities per velocity component derived in the Galactic plane gas (this work) and those derived in the Solar Neighbourhood in previous works. It is unexpected because the spatial scales of the Galactic environment sampled in this work are much larger. This suggests that the physical and chemical processes involved in the formation and destruction of the analysed species are similar in diffuse or translucent environments over the whole Galactic disk. We also find that the HCO^+ linewidths are broader than those of the CN-bearing molecules.

We compare the observed column densities to two kinds of gas phase chemical models, namely the photodissociation region (PDR) and turbulent disspation regions (TDR) models and find that: (1) the observed column densities of HCO^+ cannot be reproduced by PDR models of diffuse or translucent gas; (2) the column densities of CN-bearing species can be explained by PDR models applied to dense ($n_H > 300$ cm^{-3}) and well shielded ($A_V > 1$) molecular gas; (3) the column densities and column density ratios of HCO^+, CN, HCN, HNC, and C_2H are reproduced simultaneously by TDR models of diffuse and translucent gas, over a broad range of turbulent rates of strain (10^{-12} s$^{-1} \leqslant a \leqslant 10^{-10}$ s^{-1}), and gas densities (30 cm$^{-3} \leqslant n_H \leqslant$ 200 cm^{-3}).

Acknowledgements. We are most grateful to Eric Herbst for the valuable information regarding the grain surface chemistry of nitrogen bearing species. We also thank the referee for providing constructive comments and help in improving the content of this paper.

References

Adams, N. G., & Smith, D. 1988, Chem. Phys. Lett., 144, 11
Bechtel, H. A., Steeves, A. H., & Field, R. W. 2006, ApJ, 649, 53
Boger, G. I., & Sternberg, A. 2005, ApJ, 632, 302
Brownsword, R. A., Gatenby, S. D., Herbert, L. B., et al. 1996, J. Chem. Soc. Farday Trans., 92, 723
Carral, P., & Welch, W. J. 1992, ApJ, 385, 244

Cox, P., Güsten, R., & Henkel, C. 1988, A&A, 206, 108
Crane, P., Lambert, D. L., & Sheffer, Y. 1995, ApJS, 99, 107
Crawford, I. A. 1995, MNRAS, 277, 458
Crawford, I. A., & Williams, D. A. 1997, MNRAS, 291, 53
Crovisier, J. 1981, A&A, 94, 162
Falgarone E. 1998, in Starbursts: Trigger, Nature and Evolution, Les Houches School, ed. B. Guiderdoni, & A. Kembhavi (EPS Sciences), 41
Falgarone, E., Pineau des Forêts, G., & Roueff, E. 1995, A&A, 300, 870
Falgarone, E., Pety, J., & Hily-Blant P. 2009, A&A, 507, 355
Federman, S. R., Strom, C. J., Lambert, D. L., et al. 1994, ApJ, 424, 772
Fehsenfeld, F. C. 1976, ApJ, 209, 638
Fish, V. L., Reid, M. J., & Wilner, D. J. 2003, ApJ, 587, 701
Florescu-Mitchell, A. I., & Mitchell J. B. A. 2006, Phys. Rep., 430, 277
Flower, D. R., & Pineau des Forêts, G. 1998, MNRAS, 297, 1182
Gerin, M., Kaźmierczak, M., Jastrzebska, M., et al. 2010, A&A, submitted
Godard, B., Falgarone, E., & Pineau des Forêts G. 2009, A&A, 495, 847
Greaves, J. S., & Williams, P. G. 1994, A&A, 290, 259
Gredel, R. 1997, A&A, 320, 929
Gry, C., Boulanger, F., Nehmé, C., et al. 2002, A&A, 391, 675
Hartmann, J. 1904, ApJ, 19, 268
Haud, U., & Kalberla, P. M. W. 2007, A&A, 466, 555
Hily-Blant, P., Pety, J., & Guilloteau S. 2005, CLASS evolution: I. Improved OTF support, Tech rep., IRAM
Hily-Blant, P., Falgarone, E., & Pety, J. 2008, A&A, 481, 367
Huntress, W. T. 1977, ApJS, 33, 495
Joncas, G., Boulanger, F., & Dewdney, P. E. 1992, ApJ, 397, 165
Joulain, K., Falgarone, E., Pineau des Forêts, G., & Flower D. 1998, A&A, 340, 241
Koo, B.-C. 1997, ApJS, 108, 489
Lacour, S., Ziskin, V., Hébrard, G., et al. 2005, A&A, 627, 251
Lambert, D. L., Sheffer, Y., & Crane, P. 1990, ApJ, 359, L19
Le Petit, F., Nehmé, C., Le Bourlot, J., & Roueff, E. 2006, ApJS, 160, 506
Lesaffre, P., Gerin, M., & Hennebelle, P. 2007, A&A, 469, 949
Liszt, H., & Lucas, R. 2001, A&A, 370, 576
Liszt, H., & Lucas, R. 2002, A&A, 391, 693
Liszt, H. S., Pety, J., & Lucas, R. 2008, A&A, 486, 493
Lucas, R., & Liszt, H. 1996, A&A, 307, 237
Lucas, R., & Liszt, H. 2000, A&A, 358, 1069
Marshall, D. J., Robin, A. C., Reylé, C., Schulteis, M., & Picaud, S. 2006, A&A, 453, 635
Miville-Deschênes, M. A., Joncas, G., Falgarone, E., & Boulanger, F. 2003, A&A, 411, 109
Mookerjea, B., Casper, E., Mundy, L. G., & Looney, L. W. 2007, ApJ, 659, 447
Moskalenko, I. V., Porter, T. A., & Strong, A. W. 2006, ApJ, 640, L155
Mouri, H., & Hori, A. 2009, Fluid Dyn. Res., 41, Issue 2
Mouri, H., Hori, A., & Kawashima, Y. 2007, Phys. Fluids, 19, 055101
Neufeld, D. A., Kaufman, M. J., Goldsmith, P. F., Hollenbach, D. J., & Plume, R. 2002, ApJ, 580, 278
Nyman, L.-Å. 1983, A&A, 120, 307
Nyman, L.-Å., & Millar, T. J. 1989, A&A, 222, 231
Pan, K., Federman, S. R., Cunha, K., et al. 2004, ApJS, 151, 313
Pan, K., Federman, S. R., Sheffer, Y., & Andersson, B. G. 2005, ApJ, 633, 936
Persson, C., Black, J. H., Cernicharo, J., Goicoechea J., & the PRISMAS consortium 2010, A&A, 521, L45
Plume, R., Kaufman, M. J., Neufeld, D. A., et al. 2004, ApJ, 605, 247
Roberge, W. G., Jones, D., Lepp, S., & Dalgarno A. 1991, ApJS, 77, 287
Rydbeck, O. E. H., Kollberg, E., Hjalmarson, A., et al. 1976, ApJS, 31, 333
Semaniak, J., Minaev, B. F., Derkatch, A. M., et al. 2001, ApJS, 135, 275
Sheehan, C., Le Padellec, A., Lennard, W. N., Talbi, D., & Mitchell, J. B. A. 1999, J. Phys. B, 32, 3347
Smith, I. W. M., Herbst, E., & Chang, Q. 2004, MNRAS, 350, 323
Snow, T. P., & McCall, B. J. 2006, ARA&A, 44, 367
Talbi, D., Le Padellec, A., & Mitchell J. B. A. 2000, J. Phys. B, 33, 3631
Vastel, C., Caux, E., Ceccarelli, C., et al. 2000, A&A, 357, 994
Viggiano, A. A., Howarka, F., Albritton, D. L., et al. 1980, ApJ, 236, 492
van Dishoeck, E. F., & Black, J. H. 1988, in Rate Coefficients in Astrochemistry, ed. T. J. Millar, D. A. Williams (Dordrecht: Kluwer), 209
Wagenblast, R., & Williams, D. A. 1996, Ap&SS, 236, 257
Wagenblast, R., Williams, D. A., Millar, T. J., & Nejad, L. A. M. 1993, MNRAS, 260, 420
Weselak, T., Galazutdinov, G., Musaev, F., & Krelowski J. 2008a, A&A, 484, 381
Weselak, T., Galazutdinov, G., Musaev, F., & Krelowski J. 2008b, A&A, 479, 149
Zsargó, J., & Federman, S. R. 2003, ApJ, 589, 319

Pages 14 to 20 are available in the electronic edition of the journal at http://www.aanda.org

Appendix A: Gaussian decomposition and calculation of column densities

Tables A.1–A.4 contains the results of the Gaussian decompostion procedure that we have applied to the spectra. The column densities, given in the last columns, are derived assuming a single excitation temperature $T_{\rm ex}$ for all the levels of a given molecule as

$$N = Q(T_{\rm ex})\frac{8\pi\nu_0^3}{c^3}\frac{g_{\rm l}}{g_{\rm u}}\frac{1}{A_{\rm ul}}\left[1-{\rm e}^{-h\nu_0/kT_{\rm ex}}\right]^{-1}\int\tau\,{\rm d}\upsilon \quad (A.1)$$

where ν_0, $g_{\rm u}$, $g_{\rm l}$ and $A_{\rm ul}$ are the rest frequency, the upper and lower level degeneracies and the Einstein's coefficients of the observed transition, $Q(T_{\rm ex})$ is the partition funtion, and c is the speed of light. We also remind that for a Gaussian profile of peak opacity τ_0 and *FWHM* $\Delta\upsilon$, the opacity integral is $\int\tau\,{\rm d}\upsilon = 1/2\,\sqrt{\pi/\ln 2}\,\tau_0\,\Delta\upsilon$. For an excitation temperature of 2.73 K, Eq. (A.1) becomes

$$N({\rm HCO^+}) = 1.10\times10^{12}\int\tau\,{\rm d}\upsilon \quad {\rm cm^{-2}}, \quad (A.2)$$

$$N({\rm HNC}) = 1.78\times10^{12}\int\tau\,{\rm d}\upsilon \quad {\rm cm^{-2}}, \quad (A.3)$$

$$N({\rm HCN}) = 3.43\times10^{12}\int\tau\,{\rm d}\upsilon \quad {\rm cm^{-2}}, \quad (A.4)$$

and

$$N({\rm CN}) = 6.96\times10^{13}\int\tau\,{\rm d}\upsilon \quad {\rm cm^{-2}} \quad (A.5)$$

using the $\rm HCO^+$ $J = 0{-}1$, HNC $J = 0{-}1$, HCN $J,F = 0,1{-}1,2$, and CN $J,F1,F = 0,1/2,3/2{-}1,1/2,3/2$ transitions respectively.

Appendix B: Impact of the abscissa uncertainty on the multi-Gaussian decomposition procedure

In a spectrum, the possible velocity substructures are systematically erased due to the finite velocity resolution $\delta\upsilon$. This could be modelled as an uncertainty on the velocity position of each point. Unfortunately the errors on the abscissa are rarely included in non-linear fitting procedures because the system is considerably heavier to solve and because it often prevents convergence. To evaluate the resulting uncertainties on the fit parameters, namely the central opacity, the velocity centroid, and the *FWHM*, we apply the fitting procedure on 3000 synthetic spectra of *FWHM* $\Delta\upsilon$ varying between 0.3 and 3.4 km s^{-1} sampled with the finite spectral resolution of the observations $\delta\upsilon \sim 0.13$ km s^{-1}. A noise is added to the x-coordinates of all the spectral points. The rms of all the measured linewidths $\Delta\upsilon'$ is found to scale as

$$\frac{\delta(\Delta\upsilon')}{\Delta\upsilon} = 0.45\left(\frac{\delta\upsilon}{\Delta\upsilon}\right)^{3/2} \quad (B.1)$$

and decreases from 0.04 to 0.01 km s^{-1} as the true linewidth increases from 0.3 to 3.4 km s^{-1}. These uncertainties are smaller than (or comparable to) those inferred from the fitting procedure and the resulting errors on the column densities are at most 12%. In comparison the resulting errors on central opacities and velocity centroids are negligible.

Appendix C: Cyanides chemical network

Figures C.1 and C.2 show the main production and destruction pathways of the hydrogenation chains of carbon, nitrogen, and cyano, resulting from the PDR ($n_{\rm H} = 50$ cm^{-3}, $A_V = 0.4$) and TDR ($n_{\rm H} = 50$ cm^{-3}, $A_V = 0.4$, $a = 10^{-11}$ s^{-1}) models respectively. These figures are simplified: for each species, only the reactions which altogether contribute at least to 70 percent of the total destruction and formation rate are displayed. There is one major difference between these networks: in a UV-dominated chemical model, the cyanide chemistry is initiated by:

$$\rm CH + N \rightarrow CN + H, \quad (C.1)$$

$$\rm CH_2 + N \rightarrow HCN + H, \quad (C.2)$$

and

$$\rm NH + C^+ \rightarrow CN^+ + H; \quad (C.3)$$

while in a chemistry driven by turbulent dissipation, the hydrogenation chain of cyano is triggered by the ion-neutral reactions:

$$\rm CH^+ + N \rightarrow CN^+ + H, \quad (C.4)$$

$$\rm CH_2^+ + N \rightarrow HCN^+ + H, \quad (C.5)$$

and

$$\rm CH_3^+ + N \rightarrow HCNH^+ + H. \quad (C.6)$$

Since the pathways displayed in Figs. C.1 and C.2 depend on the chemical rates, and since the nitrogen and cyanide chemistry are still poorly known, we list the chemical rates we have adopted in our models for several reactions in Table C.1.

Table A.1. HCO^+ (0–1) absorption line analysis results.

[a] Source	v_0 (km s^{-1})	Δv (km s^{-1})	τ_0	$N(HCO^+)$ (10^{12} cm^{-2})	N_H (10^{20} cm^{-2})
G05.88-0.39	−4.92	1.13 ± 0.15	0.09 ± 0.01	0.13 ± 0.03	
G08.67-0.36	9.82	0.95 ± 0.12	1.60 ± 0.28	2.02 ± 0.58	
	11.71	1.40 ± 0.17	1.65 ± 0.28	3.08 ± 0.90	
	14.52	2.00 ± 0.18	1.41 ± 0.18	3.74 ± 0.83	
	17.76	1.17 ± 0.22	0.87 ± 0.20	1.34 ± 0.56	
	20.00	2.55 ± 0.63	1.08 ± 0.16	3.65 ± 1.45	
	22.00	1.02 ± 0.58	0.24 ± 0.17	0.32 ± 0.41	
G10.62-0.38	11.62	1.10 ± 0.12	0.43 ± 0.04	0.62 ± 0.12	
	16.38	2.35 ± 0.10	2.23 ± 0.14	6.84 ± 0.74	
	19.00	2.13 ± 0.20	1.50 ± 0.09	4.18 ± 0.64	
	22.20	2.70 ± 0.27	1.57 ± 0.13	5.57 ± 1.00	
	22.95	1.15 ± 0.45	0.82 ± 0.18	1.23 ± 0.75	
	24.98	1.65 ± 0.10	0.70 ± 0.06	1.51 ± 0.21	
	27.50	2.58 ± 0.17	1.61 ± 0.11	5.46 ± 0.74	
	29.00	1.53 ± 0.52	0.78 ± 0.20	1.56 ± 0.93	
	30.50	1.52 ± 0.32	2.09 ± 0.27	4.13 ± 1.39	
	40.91	2.60 ± 0.10	2.33 ± 0.14	7.93 ± 0.78	
	44.94	1.22 ± 0.05	1.30 ± 0.07	2.06 ± 0.21	
	46.40	0.60 ± 0.10	0.26 ± 0.04	0.20 ± 0.07	
G34.3+0.1	9.80	0.53 ± 0.22	0.38 ± 0.12	0.27 ± 0.19	
	10.60	0.57 ± 0.12	1.86 ± 0.61	1.38 ± 0.72	
	11.70	1.37 ± 0.18	1.82 ± 0.39	3.34 ± 1.14	
	14.07	0.37 ± 0.08	0.77 ± 0.23	0.38 ± 0.20	
	27.00	1.02 ± 0.13	1.19 ± 0.20	1.61 ± 0.47	
	27.75	1.83 ± 0.32	0.45 ± 0.09	1.10 ± 0.41	
	48.30	2.23 ± 0.20	0.94 ± 0.10	2.80 ± 0.54	
W49N	33.20	0.65 ± 0.03	0.44 ± 0.02	0.34 ± 0.02	3.0
	33.70	2.23 ± 0.03	0.63 ± 0.01	1.67 ± 0.02	10.5
	36.50	1.67 ± 0.12	0.29 ± 0.01	0.60 ± 0.03	7.8
	38.50	1.75 ± 0.08	0.91 ± 0.01	1.88 ± 0.03	8.2
	39.70	1.47 ± 0.02	2.01 ± 0.03	3.47 ± 0.05	6.9
	50.92	1.65 ± 0.10	0.35 ± 0.01	0.68 ± 0.02	7.8
	53.40	1.23 ± 0.10	0.30 ± 0.02	0.43 ± 0.03	5.8
	54.00	3.38 ± 0.15	0.51 ± 0.01	2.03 ± 0.04	15.9
	56.70	2.35 ± 0.07	0.69 ± 0.01	1.91 ± 0.03	11.0
	59.55	2.35 ± 0.05	1.89 ± 0.02	5.24 ± 0.07	11.0
	60.80	0.88 ± 0.05	0.77 ± 0.05	0.80 ± 0.06	4.1
	62.65	2.95 ± 0.03	1.48 ± 0.01	5.16 ± 0.05	13.9
	66.21	1.85 ± 0.07	0.19 ± 0.01	0.41 ± 0.01	8.7
	68.58	1.80 ± 0.10	0.24 ± 0.01	0.52 ± 0.01	8.5
	71.11	2.25 ± 0.20	0.07 ± 0.00	0.19 ± 0.01	10.6
W51	3.80	0.47 ± 0.12	0.10 ± 0.02	0.06 ± 0.03	1.0
	5.10	1.23 ± 0.05	0.72 ± 0.02	1.14 ± 0.08	2.7
	6.25	0.65 ± 0.03	1.05 ± 0.06	0.87 ± 0.10	1.4
	6.85	2.01 ± 0.05	0.70 ± 0.02	1.80 ± 0.10	4.4
	12.71	1.67 ± 0.18	0.10 ± 0.01	0.20 ± 0.04	3.7
[b] Source	v_{min} (km s^{-1})	v_{max} (km s^{-1})	$\int \tau dv$ (km s^{-1})	$N(HCO^+)$ (10^{12} cm^{-2})	
G10.62-0.38	13.6	15.2	0.77 ± 0.08	0.94 ± 0.10	
	31.0	33.0	3.77 ± 0.31	4.63 ± 0.38	
	33.3	34.7	1.81 ± 0.15	2.23 ± 0.18	
	34.7	36.0	1.74 ± 0.16	2.13 ± 0.19	
	36.0	37.5	3.10 ± 0.29	3.82 ± 0.36	
	37.5	40.0	>6.27	>7.71	
W49N	41.0	47.0	0.90 ± 0.03	1.00 ± 0.04	

Notes. [(a)] Multi-Gaussian decomposition. The column densities are derived assuming the excitation temperatures given in Table 3. [(b)] Failure of the multi-gaussian decomposition. Column densities are inferred from the integral of the opacity assuming the excitation temperatures given in Table 3. [(c)] Determined from the average total hydrogen column density per unit velocity $N_H/\Delta v$ = 2.2 and 4.7×10^{20} cm^{-2}/km s^{-1} toward W51 and W49N respectively.

Table A.2. HNC (0–1) absorption line analysis products.

[a] Source	v_0 (km s^{-1})	Δv (km s^{-1})	τ_0	N(HNC) (10^{12} cm^{-2})
G10.62-0.38	11.62	1.72 ± 0.22	0.19 ± 0.02	0.72 ± 0.17
	14.42	1.23 ± 0.42	0.09 ± 0.02	0.24 ± 0.14
	16.38	1.30 ± 0.05	1.43 ± 0.07	4.02 ± 0.33
	19.16	2.01 ± 0.15	0.50 ± 0.03	2.19 ± 0.27
	22.20	2.15 ± 0.28	0.38 ± 0.06	1.76 ± 0.51
	22.95	1.17 ± 0.13	1.21 ± 0.08	3.06 ± 0.57
	24.98	2.05 ± 0.35	0.13 ± 0.02	0.60 ± 0.18
	27.80	1.50 ± 0.07	1.18 ± 0.08	3.82 ± 0.44
	29.10	1.32 ± 0.18	1.16 ± 0.10	3.84 ± 0.85
	30.25	1.13 ± 0.07	1.23 ± 0.10	3.02 ± 0.41
	31.90	2.31 ± 0.37	0.45 ± 0.03	2.28 ± 0.50
	34.00	1.08 ± 0.22	0.32 ± 0.04	0.76 ± 0.25
	35.35	1.02 ± 0.13	0.53 ± 0.05	1.16 ± 0.26
	36.51	1.22 ± 0.10	0.81 ± 0.05	2.12 ± 0.31
	38.80	2.16 ± 0.18	0.72 ± 0.03	3.38 ± 0.45
	40.91	1.30 ± 0.05	2.16 ± 0.14	6.10 ± 0.63
	44.94	1.30 ± 0.10	0.34 ± 0.03	0.95 ± 0.15
G34.3+0.1	10.60	0.58 ± 0.13	0.15 ± 0.03	0.19 ± 0.08
	11.80	1.45 ± 0.15	0.28 ± 0.02	0.85 ± 0.15
	27.00	1.05 ± 0.07	0.48 ± 0.03	1.06 ± 0.13
W49N	33.50	1.77 ± 0.17	0.12 ± 0.01	0.39 ± 0.06
	38.50	1.68 ± 0.10	0.22 ± 0.01	0.70 ± 0.08
	39.70	0.95 ± 0.02	1.46 ± 0.04	2.63 ± 0.11
	50.92	0.53 ± 0.15	0.06 ± 0.01	0.06 ± 0.03
	54.00	2.85 ± 0.32	0.09 ± 0.01	0.47 ± 0.09
	56.70	1.78 ± 0.18	0.10 ± 0.01	0.32 ± 0.06
	59.40	2.01 ± 0.08	0.44 ± 0.01	1.67 ± 0.11
	60.90	0.97 ± 0.13	0.08 ± 0.01	0.15 ± 0.04
	62.60	2.15 ± 0.08	0.39 ± 0.01	1.58 ± 0.11
[b] Source	v_{min} (km s^{-1})	v_{max} (km s^{-1})	$\int \tau dv$ (km s^{-1})	N(HNC) (10^{12} cm^{-2})
G10.62-0.38	46.0	47.0	<0.03	<0.07
G34.3+0.1	9.0	10.1	<0.03	<0.06
	13.3	14.7	<0.04	<0.07
	46.0	50.0	<0.06	<0.11
W49N	35.0	37.0	0.09 ± 0.02	0.16 ± 0.04
	41.0	47.0	0.11 ± 0.04	0.19 ± 0.06
	65.0	67.3	0.10 ± 0.02	0.18 ± 0.04
	67.3	69.7	0.07 ± 0.02	0.12 ± 0.04
	69.7	72.5	<0.02	<0.04
W51	3.0	5.5	0.09 ± 0.05	0.17 ± 0.10
	5.5	9.5	0.09 ± 0.06	0.18 ± 0.12
	11.0	14.0	<0.06	<0.11

Notes. [(a)] Same as Table A.1. [(b)] Same as Table A.1.

Table A.3. HCN (0–1) absorption line analysis products.

[a] Source	v_0 (km s^{-1})	Δv (km s^{-1})	τ_0	N(HCN) (10^{12} cm^{-2})
G10.62-0.38	44.97	0.92 ± 0.03	1.45 ± 0.07	5.40 ± 0.45
G34.3+0.1	10.10	1.00 ± 0.15	0.16 ± 0.02	0.66 ± 0.18
	10.60	0.32 ± 0.03	0.40 ± 0.04	0.53 ± 0.12
	11.80	1.22 ± 0.05	0.85 ± 0.03	4.27 ± 0.33
	27.00	0.57 ± 0.02	1.47 ± 0.06	3.44 ± 0.24
	27.75	0.55 ± 0.05	0.35 ± 0.03	0.81 ± 0.14
W49N	33.40	1.43 ± 0.05	0.42 ± 0.01	2.20 ± 0.06
	38.50	1.22 ± 0.03	0.65 ± 0.01	2.91 ± 0.06
	39.70	0.87 ± 0.02	3.94 ± 0.06	12.51 ± 0.18
	51.00	1.00 ± 0.17	0.11 ± 0.01	0.40 ± 0.11
	54.00	2.50 ± 0.20	0.24 ± 0.01	2.23 ± 0.21
	56.60	1.83 ± 0.15	0.28 ± 0.01	1.85 ± 0.22
	59.40	1.50 ± 0.05	1.35 ± 0.02	7.44 ± 0.10
	60.90	0.83 ± 0.05	0.64 ± 0.02	1.96 ± 0.05
	62.55	1.83 ± 0.05	1.15 ± 0.01	7.73 ± 0.09
W51	5.00	0.93 ± 0.12	0.17 ± 0.02	0.63 ± 0.14
	6.80	1.27 ± 0.12	0.20 ± 0.02	1.02 ± 0.17
[b] Source	$v_{\rm min}$ (km s^{-1})	$v_{\rm max}$ (km s^{-1})	$\int \tau {\rm d}v$ (km s^{-1})	N(HCN) (10^{12} cm^{-2})
W49N	69.7	72.5	0.03 ± 0.03	0.18 ± 0.15
W51	11.0	14.0	<0.04	<0.27

Notes. [(a)] Same as Table A.1. [(b)] Same as Table A.1.

Table A.4. CN (0–1) absorption line analysis products.

[a] Source	v_0 (km s^{-1})	Δv (km s^{-1})	τ_0	N(CN) (10^{13} cm^{-2})
G10.62-0.38	11.62	0.92 ± 0.18	0.16 ± 0.02	1.19 ± 0.35
	16.30	1.20 ± 0.03	1.16 ± 0.03	11.10 ± 0.63
	19.16	1.03 ± 0.10	0.47 ± 0.02	3.91 ± 0.59
	22.20	1.83 ± 0.00	0.32 ± 0.02	4.75 ± 0.35
	22.90	0.87 ± 0.05	1.16 ± 0.05	8.04 ± 0.87
	27.80	1.47 ± 0.05	1.23 ± 0.04	14.34 ± 1.05
	29.10	0.78 ± 0.07	0.99 ± 0.07	6.20 ± 0.92
	30.20	1.10 ± 0.05	1.39 ± 0.06	12.28 ± 1.05
	31.80	2.10 ± 0.28	0.38 ± 0.02	6.43 ± 1.12
	34.00	1.22 ± 0.28	0.19 ± 0.02	1.88 ± 0.63
	35.35	0.68 ± 0.07	0.44 ± 0.03	2.38 ± 0.38
	36.61	1.40 ± 0.13	0.50 ± 0.02	5.56 ± 0.77
	38.80	1.63 ± 0.10	0.66 ± 0.02	8.65 ± 0.84
	40.75	1.35 ± 0.03	1.70 ± 0.05	18.30 ± 0.95
	44.94	0.83 ± 0.08	0.22 ± 0.04	1.43 ± 0.41
G34.3+0.1	27.00	0.68 ± 0.12	0.86 ± 0.17	1.79 ± 0.66
W49N	33.30	1.83 ± 0.12	0.13 ± 0.01	1.82 ± 0.22
	38.40	1.77 ± 0.08	0.23 ± 0.01	3.02 ± 0.27
	39.60	0.85 ± 0.02	1.18 ± 0.03	7.43 ± 0.29
	59.20	1.98 ± 0.08	0.27 ± 0.01	3.98 ± 0.34
	62.40	1.62 ± 0.07	0.32 ± 0.01	3.77 ± 0.31
[b] Source	$v_{\rm min}$ (km s^{-1})	$v_{\rm max}$ (km s^{-1})	$\int \tau {\rm d}v$ (km s^{-1})	N(CN) (10^{13} cm^{-2})
G10.62-0.38	13.6	15.2	0.18 ± 0.06	0.85 ± 0.29
	24.0	26.0	0.26 ± 0.07	1.29 ± 0.34
	46.0	47.0	<0.04	<0.21
G34.3+0.1	9.0	10.1	0.20± 0.13	1.54 ± 1.01
	10.1	11.0	<0.11	<0.84
	11.0	13.0	0.48 ± 0.18	3.63 ± 0.14
	13.3	14.7	0.15 ± 0.14	1.12 ± 1.05
	46.0	50.0	<0.19	<1.46
W49N	35.0	37.0	<0.03	<0.13
	41.0	47.0	<0.05	<0.22
	50.0	52.0	<0.03	<0.13
	52.5	55.5	0.09 ± 0.04	0.41 ± 0.17
	55.5	57.9	0.07 ± 0.03	0.32 ± 0.14
	60.3	61.3	0.09 ± 0.02	0.41 ± 0.10
W51	3.0	5.5	0.13 ± 0.08	0.97 ± 0.56
	5.5	9.5	<0.09	<0.69
	11.0	14.0	<0.08	<0.59

Notes. [(a)] Same as Table A.1. [(b)] Same as Table A.1.

Table C.1. Rates k of the main reactions of the cyanide chemistry.

Reaction				α	β	γ	Ref.
CN	+ hν	→ C	+ N	4.64 (–10)	0.00	3.6	*a*
HCN	+ hν	→ CN	+ H	5.70 (–10)	0.00	2.6	*a*
HNC	+ hν	→ CN	+ H	5.70 (–10)	0.00	2.6	*a*
$HCNH^+$	+ e^-	→ HCN	+ H	9.45 (–08)	–0.65	0.0	*b*, *c*
$HCNH^+$	+ e^-	→ HNC	+ H	9.45 (–08)	–0.65	0.0	*b*, *c*
$HCNH^+$	+ e^-	→ CN	+ 2H	9.10 (–08)	–0.65	0.0	*b*, *c*
$HCNH^+$	+ e^-	→ CN	+ H_2	1.80 (–08)	–0.65	0.0	*b*, *c*
H_2NC^+	+ e^-	→ HNC	+ H	1.75 (–07)	–0.50	0.0	*d*
H_2NC^+	+ e^-	→ CN	+ H_2	1.75 (–07)	–0.50	0.0	*d*
HNC^+	+ e^-	→ CN	+ H	3.90 (–07)	–1.00	0.0	*e*, *f*
HCN^+	+ e^-	→ CN	+ H	3.90 (–07)	–1.00	0.0	*e*
CH_3^+	+ N	→ HCN^+	+ H_2	2.20 (–11)	0.00	0.0	*g*
CH_3^+	+ N	→ $HCNH^+$	+ H	2.20 (–11)	0.00	0.0	*g*
CH_3^+	+ N	→ H_2NC^+	+ H	2.20 (–11)	0.00	0.0	*g*
CH_2^+	+ N	→ HCN^+	+ H	4.70 (–10)	0.00	0.0	
CH_2^+	+ N	→ HNC^+	+ H	4.70 (–10)	0.00	0.0	
CH^+	+ N	→ CN^+	+ H	1.90 (–10)	0.00	0.0	*h*
CH_2	+ N	→ HCN	+ H	3.95 (–11)	0.17	0.0	*i*
CH	+ N	→ CN	+ H	2.00 (–10)	0.00	0.0	*j*
C^+	+ NH	→ CN^+	+ H	7.80 (–10)	0.00	0.0	
C^+	+ NH_2	→ HCN^+	+ H	1.10 (–09)	0.00	0.0	
HCN^+	+ H_2	→ $HCNH^+$	+ H	9.00 (–10)	0.00	0.0	*k*
HNC^+	+ H_2	→ $HCNH^+$	+ H	9.00 (–10)	0.00	0.0	*k*

Notes. The photoreaction rates writte $k = \alpha \cdot \exp(-\gamma A_V)$ while all the other reaction rates are derived as $k = \alpha \cdot (T/300\ \mathrm{K})^{\beta} \exp(-\gamma/T)$ where T is the effective temperature (Zsargó & Federman 2003). Numbers in parenthesis are power of 10.

References. [(a)] Roberge et al. (1991); [(b)] Florescu-Mitchell & Mitchell (2006); [(c)] Semaniak et al. (2001); [(d)] Adams & Smith (1988); [(e)] Sheehan et al. (1999); [(f)] Talbi et al. (2000); [(g)] Fehsenfeld (1976); [(h)] Viggiano et al. (1980); [(i)] Smith et al. (2004); [(j)] Brownsword et al. (1996); [(k)] Huntress (1977).

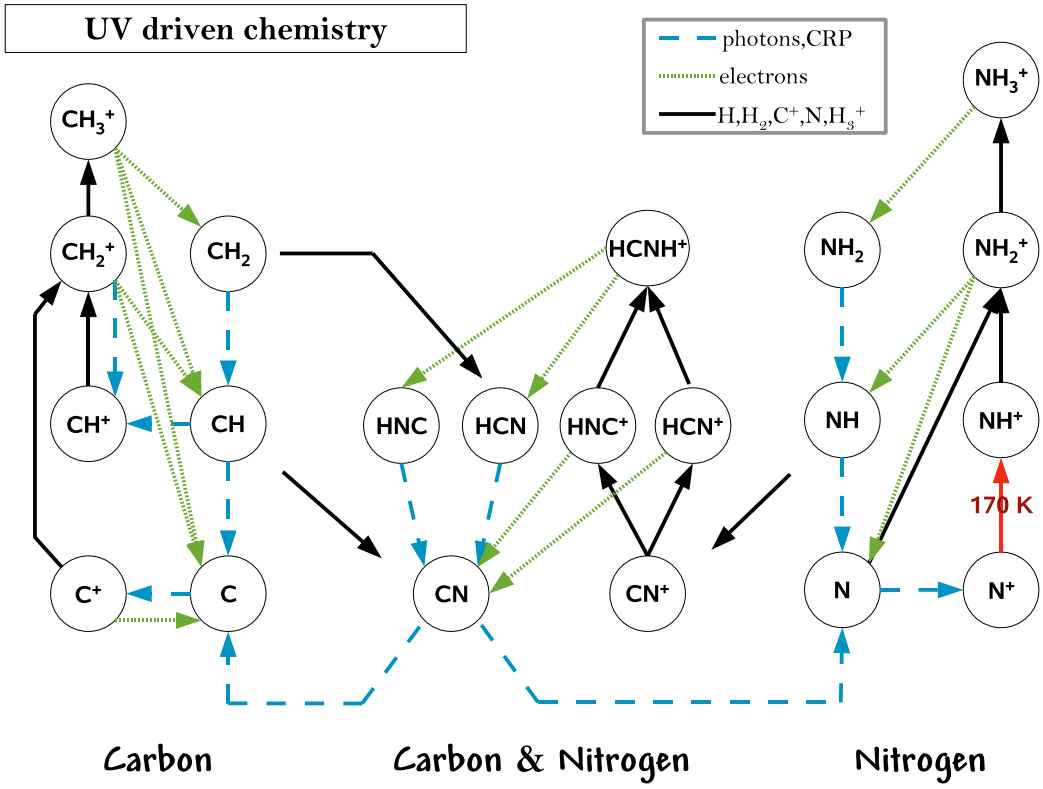

Fig. C.1. Chemical network of a UV-dominated chemistry: $n_H = 50$ cm^{-3} and $A_V = 0.4$. This figure is simplified: for each species, only the reactions which altogether contribute at least to 70 percent of the total destruction and formation rate are displayed. The red arrow show the endoenergetic reactions with the energy involved.

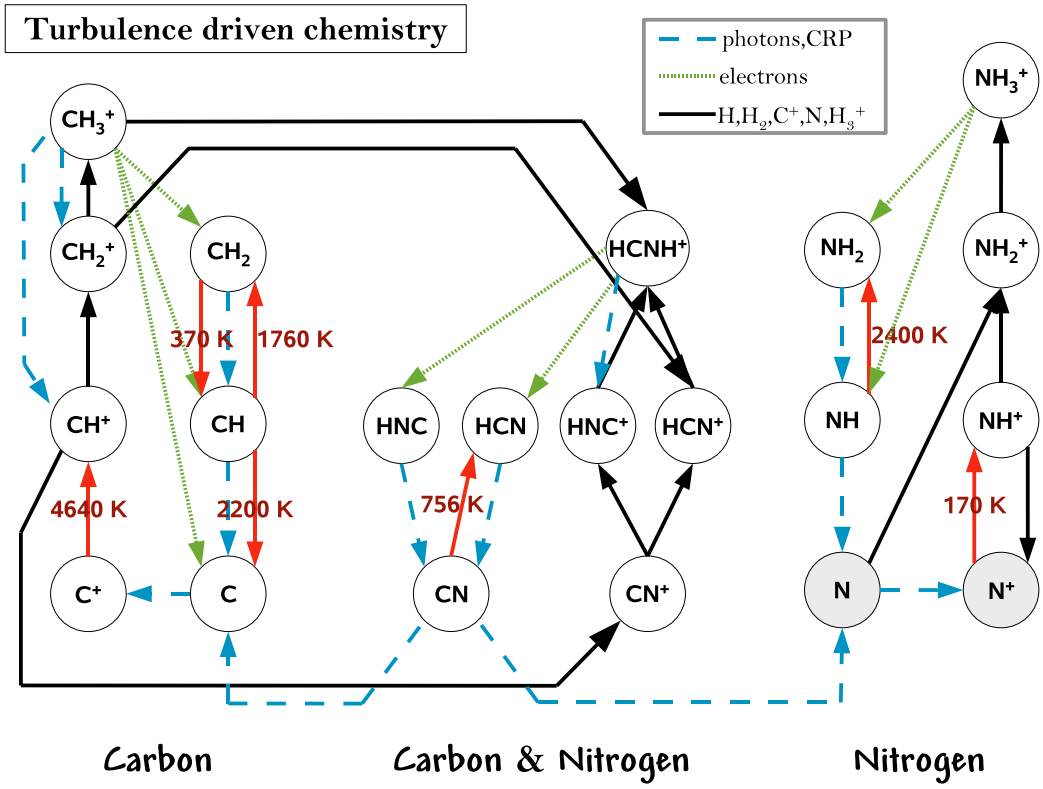

Fig. C.2. Same as Fig. C.1 for a turbulence-dominated chemistry: $n_H = 50$ cm^{-3}, $A_V = 0.4$ and $a = 10^{-11}$ s^{-1}. For the sake of simplicity, the main destruction route of N ($N + CH_2^+ \rightarrow HCN^+ + H$) and the main formation pathway of N^+ (photodissociation of NO^+) are not displayed here: those two species are therefore highlighted.